SENSITIVITY STUDIES FOR ARGUS 1000 MICRO-SPECTROMETER: MEASUREMENTS OF ATMOSPHERIC TOTAL COLUMN CARBON DIOXIDE BY REFLECTED SUNLIGHT

NAIF ZAID M. ALSALEM

A THESIS SUBMITTED TO THE FACULTY OF GRADUATE STUDIES IN PARTIAL FULLFILLMENT OF THE REQUIREMENTS FOR THE DEGREE OF

MASTER OF SCIENCE

GRADUATE PROGRAMM IN PHYSICS AND ASTRONOMY
York University
Toronto, Ontario
March 2016

© NAIF ZAID M. ALSALEM, 2016

Abstract

A sensitivity analysis of the atmospheric boundary layer (ABL) and the atmospheric total column carbon dioxide was performed. The absorption of reflected solar radiation from the atmosphere and Earth's surface near 1.58 μm is utilized in this study. The CO_2 near infrared (NIR) bands at 1.58 μm and 1.60 μm are located within the Argus 1000 spectrometer spectral range, 1.0−1.7μm. The model findings suggest that Argus 1000 spectrometer signal-to-noise ratio (SNR) must be 2000:1 to detect a 1% CO_2 change in the boundary layer (0-2 km). Argus 1000 spectrometer with its current SNR (~ 1520:1) can detect approximately 1.31% CO_2 change in the boundary layer (ABL).

Two solar radiance paths were considered using GENSPECT, a line-by-line radiative transfer model, to examine the solar radiance spectra seen by the sensor. In path one, sunlight is assumed to travel through a longer path length in the atmosphere and reflect off the ground back to space. In path two, the solar beam is assumed to travel through a shorter path length and reflect off a cloud layer that is 4 km above the ground. The model findings suggest that the ratio between the solar radiances in both paths is approximately 4.5. The radiance change in both paths was examined for a 1% CO_2 perturbation in the boundary layer. The effect of the presence of clouds on both solar radiation and CO_2 absorption is also analyzed using flight data collected by the Argus 1000 spectrometer over cloudy and cloud-free scenes. The finding shows that CO_2 absorption in a clear sky condition is approximately 5.3% higher than when clouds are present.

Dedication

I sincerely dedicated this work to:

My Father

The one who taught me and dedicated his entire life for my betterment. The one who struggled in this tough life and went through trails and hardship just to preserve a bright future for me.

My Mother

The one who has been through every single hardship with me. The one who remembered me in her late-night prayers. The one who without her mere presence I would not have been in this stage of my life.

My Brothers and Sisters

Who stood with me during my educational journey to the land of opportunities, Canada.

Acknowledgements

First and foremost, I would like to express my deepest gratitude and appreciation to my Ph.D. supervisor, Space Engineer, Prof. Brendan (Ben) Quine for his unlimited and sincere support, his restless effort to assist me in understanding complicated topics, and his patience throughout my master's research period. Prof. Brendan Quine opened the knowledge door for me to become a successful and professional graduate student in the field. He provided me with all the means necessary to carry out my Master's research and encouraged me to get involved in many scientific experiments to strengthen my experimental ability and enhance my laboratory experience. This thesis would not have been possible without Prof. Quine's guidance and constant encouragement throughout my research work. Moreover, during the most difficult and critical times while researching in this field, he gave me the moral support and backed me up with all means necessary to move on. Simply put, he has given me the golden opportunity to do research under his supervision and guidance.

I would like also to extend my thanks to my committee member Ph.D. Astronomer, Prof. Marshall McCall for his guidance and encouragement throughout the research evaluation meetings. I would like also to thank Prof. George Zhu for being in my advisory committee. I also thank my team members: Rehan Siddiqui for his sincere discussions and continuous suggestions, and Catherine Tsouvaltsidis for her sincere assistance at the beginning of my degree and during my research work as well as her guidance while I was writing the Systems Tool Kit (STK) certification exam.

I would like to acknowledge the effort of Guy Benari when he was directed by Prof. Brendan Quine to train me on the Systems Tool Kit (STK) which is of significant importance in

creating the observation tables for Argus 1000 spectrometer and determine the global targets for Argus.

It is with immense gratitude that I acknowledge the precious time that Mourad Amara, Ph.D. student at Lassonde School of Engineering has dedicated for me to explain and demonstrate some physics-related topics such as special relativity issues of time-delay between the GPS satellites and their ground stations as well as his valuable information in the fields of Time and Cosmology. He invested valuable time trying to explain to me the CEMOS various technology and digital signal processing (DSP) methods.

Finally, I offer my humble thanks and devotion to my family without whose infinite support this endeavor would not have been possible and achieved.

Table of Contents

ABSTRACT II

DEDICATION III

ACKNOWLEDGEMENTS IV

LIST OF TABLES VII

LIST OF FIGURES VIII

LIST OF ACRONYMS XI

1.0 INTRODUCTION 1

1.1 THESIS STATEMENT 3
1.2 THESIS OUTLINE 4

2.0 BACKGROUND 6

2.1 OTHER GREENHOUSE GAS MEASUREMENTS FROM SPACE 10
2.2 SENSITIVITY STUDIES FOR SPACE-BASED MEASUREMENTS OF ATMOSPHERIC TOTAL COLUMN CO_2 20
2.3 CANX-2 MISSION TO SPACE (CANADIAN ADVANCED NANOSATELLITE EXPERIMENT-2) 22
2.3.1 PAYLOADS 24
2.3.2 LAUNCH OF CANX-2 SATELLITE 25
2.4 ARGUS 1000 SPECTROMETER 27
2.4.1 ARGUS 1000 SPECTROMETER DESIGN 30
2.4.2 DETECTOR SYSTEM 31
2.4.3 OPTICAL DESIGN 32
2.4.4 INSTRUMENT OPERATION 35
2.4.5 POTENTIAL INSTRUMENT IMPROVEMENTS 38
3.0 MEASUREMENTS STRATEGY 39
3.1 THE RADIATIVE TRANSFER EQUATION 39
3.2 THE GENSPECT RADIATIVE TRANSFER MODEL WITH SELECTABLE INTERPOLATION ERROR TOLERANCE 41
3.3 THE SENSITIVITY ANALYSIS METHODOLOGY 42

4.0 RESULTS AND DISCUSSION 44

4.1 ARGUS 1000 SPECTROMETER SPECTRAL RANGE 44
4.2 MEASUREMENT SENSITIVITY TO CO_2 CONCENTRATION CHANGE 47
  4.2.1 Argus 1000 Signal-to-Noise Ratio 53
4.3 SOLAR RADIATION PATH SCENARIOS 57
4.4 EFFECTS OF CLOUDS ON SOLAR RADIATION AND CO_2 ABSORPTION 58

5.0 CONCLUSION 63

5.1 FUTURE WORK 65

REFERENCES 66

List of Tables

Table 1: Major greenhouse gas content in the air, growth rate for 1995 to 2005 decade and radiative forcing [IPCC 2007, Chapter 2]. 7

Table 2: Concentration and Radiative forcing values of GHGs in 2005 and 2011 [IPCC 2014, Chapter 8]. 7

Table 3: Comparison between some selected parameters of the TIR instruments IASI, AIRS and HIRS [Clerbaux *et al*., 2009; Bréon & Ciais, 2010;Garand *et al*., 2001]. 12

Table 4: Characteristics of SCIAMACHY, TANSO and GOMOS instruments 14

Table 5: OCO-2 and Argus main technical specifications 19

Table 6: Gas species observed by IR Argus 1000 spectrometer and their absorption bands. 28

Table 7: Argus 1000 specifications [Argus manual, 2010] 30

Table 8: List of the selected targets for week 100 of January 19th, 2015 36

Table 9: Argus 1000 spectrometer Data Packet Format for CanX-2 flight model. 38

Table 10: Parameters used in the analysis 47

Table 11: Absorption minima corresponding to different SZAs. 53

Table 12: Mean values, STDs and SNRs of all pixels shown in Figure 37 56

Table 13: Model parameters used in the path scenario calculation. 58

Table 14: Geolocation details for the weeks and passes in Figure 41. 61

Table 15: Model parameters used in the fitting in Figure 42 63

List of Figures

Figure 1: Concentration of CO_2 is approaching 400 ppm for the first time in history. Mauna Loa Observatory, Hawaii: [http://www.esrl.noaa.gov/] ----------2

Figure 2: Argus 1000 in the space facility at York University [http://www.thoth.ca/] ----------3

Figure 3: Comparison between GHGs concentration in 2005 and 2011 according to IPCC 2014 data.----------8

Figure 4: Satellite remote sensing is capable of providing more frequent and repetitive coverage over a large area than other observational means. Figure courtesy of R. He, Hainan University----------9

Figure 5: Partly integrated CanX-2 spacecraft [Courtesy: UTIAS] ---------- 23

Figure 6: Accommodation of subsystems in the CanX-2 bus [Courtesy: UTIAS] ---------- 23

Figure 7: CanX-2 Mission Patch [Courtesy: UTIAS]---------- 24

Figure 8: The science payloads. The atmospheric spectrometer, GPS antenna and receiver, and advanced surface material experiment [Courtesy: UTIAS].---------- 25

Figure 9: PSLV-C9 upper stage and the position of CanX-2 [Courtesy: ISRO] ---------- 26

Figure 10: (A) PSLV-C9 on its way to the launch pad, (B) PSLV-C9 on the launch pad, April 28th, 2009 [Courtesy: UTIAS/ISRO]. ---------- 26

Figure 11: Nadir viewing geometry of Argus 1000 spectrometer. [Image credit: Jagpal, 2012]---------- 28

Figure 12: Argus 1000 spectrometer commercial unit shown at the Space Engineering Laboratory, York University. ---------- 29

Figure 13: Argus 1000 External Dimensions [Courtesy: Thoth Technology Inc., 2010] . ---------- 31

Figure 14: Detector Quantum Efficiency for 1.7 μm device.---------- 32

Figure 15: Schematic of an integrating transimpedance amplifier. ---------- 32

Figure 16: The internal structure of the Argus 1000 spectrometer. ---------- 33

Figure 17: The optical design layout of Argus. The main mirror is 35 mm and the input mirror is 15 mm. The grating is 300 g/mm.---------- 34

Figure 18: Argus functional diagram showing optics (blue), electronics layer (brown), cooler components layer (red), software layer (green) [Argus Manual, 2010].---------- 34

Figure 19: Sample of Argus targets in STK. ---------- 35

Figure 20: Some of Argus targets around the globe and CanX-2 passes over them.---------- 36

Figure 21: Data files provided by UTIAS for each pass in every observational campaign. ---------- 37

Figure 22: Illustration of energy transportation (Beer–Lambert Law). ---------- 40

Figure 23: Solar radiation when strikes the Earth's surface at a large zenith angle (A) and when it makes a small zenith angle (B). ---------- 43

Figure 24: Argus Synthetic Spectra in GENSPECT and the positions of absorbing gases ---------- 45

Figure 25: Argus synthetic smoothed radiance (W m^{-2} sr^{-1} $(cm^{-1})^{-1}$) in the model and the gas absorption band positions in the spectral range from1 to 1.7 microns. ---------- 45

Figure 26: Carbon dioxide bands at 1.58 and 1.60 μm. Notice the CO_2 concentration 0 ppm (dashed blue line) and 360 ppm (red line). -- 46

Figure 27: One way (space-to-ground) radiation transmittance of CO_2 (blue line) and H_2O (red line) in the 1568-1582 nm band at Nadir viewing geometry. 1976 U.S Standard Atmosphere was used in the calculation. Notice the minimal interference of H_2O in this band-- 46

Figure 28: Top panel, the Nadir viewing back-to-space radiance (mW m^{-2} sr^{-1} $(cm^{-1})^{-1}$) at solar zenith angle 30° in the whole atmospheric column (0–50 km); bottom panel, the smoothed back-to-space radiance at SZA 30° in the whole column. -- 48

Figure 29: Top panel, the radiance sensitivity to ~0.28% (1-ppmv) CO_2 concentration increase in the whole column; bottom panel, the smoothed radiance sensitivity to 1 ppm mixing ratio change in the wholecolumn. ----- 48

Figure 30: Top panel, the Nadir viewing back-to-space radiance (mW m^{-2} sr^{-1} $(cm^{-1})^{-1}$) at solar zenith angle 30° in the atmospheric boundary layer ABL (0–2 km); bottom panel, the smoothed back-to-space radiance at SZA 30° in the ABL. --- 50

Figure 31: Top panel, the radiance sensitivity to 1% (3.6 ppmv) CO_2 concentration increase in the atmospheric boundary layer ABL (0–2 km); bottom panel, the smoothed radiance sensitivity to a 3.6 ppm mixing ratio change in the ABL. -- 50

Figure 32: Top panel; comparison between radiance sensitivities to 0.28% (1-ppmv) CO_2 concentration increase (red line) in the whole column (0-50 km) and to a 1% (3.6 ppm) CO_2 mixing ratio increase (blue line) in the boundary layer (0-2 km). Bottom panel; smoothed spectra of the comparison in the top panel. Both radiance changes were calculated for SZA 30°. -- 51

Figure 33: Top panel, the back-to-space radiance (mW m^{-2} sr^{-1} $(cm^{-1})^{-1}$) at SZA of 30°. Bottom panel, the smoothed top-of-the atmosphere radiance at the same SZA.-- 52

Figure 34: Top panel, the back-to-space radiance (mW m^{-2} sr^{-1} $(cm^{-1})^{-1}$) at SZA of 80°. Bottom panel, the smoothed top-of-the atmosphere radiance at the same SZA.-- 52

Figure 35: Laboratory experiment setup top view (left) and mirror and light source (right). [Image credit: Catherine Tsouvaltsidis & Naif Al Salem] -- 53

Figure 36: Instrument signal at pixel number 242. --- 55

Figure 37: Instrument signal at pixel 240 (top left), 241 (bottom left), 246 (top right) and 247 (bottom right). ------ 55

Figure 38: Illustration of possible scenarios as solar radiation passes through the atmosphere and back to space to reach the sensor. I_{dir} is the solar radiation beam directly reflected by the Earth's surface toward the sensor field of view (FOV). I_{rfc} is the solar beam reflected off clouds.-- 57

Figure 39: Synthatic solar beams reflected off ground (left panel) and off cloud (right panel) at SZA of 30°. ------- 58

Figure 40: The full spectrum of cloudy and clear scenes (first row) for week 41 pass 34, week 9 pass 36 and week 77 pass 28, respectively. Second row shows normalized cloudy and clear spectra at the CO_2 band 1575 nm. The third row shows the actual cloud cover. [Cloud imagery by Reto Stockli, NASA's Earth Observatory http://neo.sci.gsfc.nasa.gov/] -- 60

Figure 41: Synthetic (blue) and observed (red) radiance profiles. -- 62

Figure 42: The CO_2 concentration level on the 28th of August 2013 as reported from the National Oceanic and Atmospheric Administration web. Graph Credit [http://www.esrl.noaa.gov/gmd/ccgg/trends/graph.html]. --- 62

List of Acronyms

ABL	Atmospheric Boundary Layer
ACE	Atmospheric Chemistry Experiment
AIRS	Atmospheric Infra-Red Sounder
AMSU	Advanced Microwave Sounder Unit
AVHRR	Advanced Very High Resolution Radiometer
CanX-2	Canadian Advanced Nano-space eXperiment-2
CFC	Chlorofluorocarbons
ESA	European Space Agency
ERS	European Remote Sensing Satellite
FOV	Field of View
GHG	Greenhouse Gas
GOME	Global Ozone Monitoring Experiment
GOMOS	Global Ozone Monitoring by Occultation of Stars
GOSAT	Greenhouse gases Observing SATellite
GPS	Global Positioning System
HIRS	High Resolution Infrared Radiation Sounder
HSB	Humidity Sounder for Brazil
IASI	Infrared Atmospheric Sounding Interferometer
IPCC	Intergovernmental Panel on Climate Change
IR	Infra-Red
ISRO	Indian Space Research Organization

JAXA	Japan Aerospace Exploration Agency
LEO	Low Earth Orbit
MIPAS	Michelson Interferometer for Passive Atmospheric Sounding
MODIS	Moderate-resolution Imaging Spectroradiometer
NASA	National Aeronautics and Space Administration
NIR	Near Infra-Red
NOAA	National Oceanic and Atmospheric Administration
OCO	Orbiting Carbon Observatory
PBL	Planetary Boundary Layer
PPB	Parts Per Billion
PPM	Parts Per Million
PSLV	Polar Satellite Launch Vehicle
RF	Radiative Forcing
SNR	Signal to Noise Ratio
STK	Systems Tool Kit
SWIR	Short-Wave Infra-Red
SZA	Solar Zenith Angle
TIRS	Thermal Infrared Sensor

1.0 Introduction

The global community is facing climate change, which is recognized as a human problem of environment. The environment is continuously responding to human interference with the climate system and for this reason many countries around the globe are establishing new regulations and policies to restrain the effect of human activities on the environment. Climate-control regulations and assessment require a precise determination of the sources, sinks, and concentration of the atmospheric constituents related to climate change.

The Sun is the major source of energy for almost all life on Earth. Solar radiation travels in the vacuum and partially passes through the atmosphere, striking the Earth's surface, causing warmth to all objects on the ground. The Earth's surface then re-emits the absorbed heat as infrared radiation, which is then partially absorbed by atmospheric gases [Tyndall, 1861]. The atmosphere releases some of the absorbed radiation back to Earth as infra-red (IR) radiation that can disturb the natural radiation balance, causing, for example, the climate system to store surplus solar energy, eventually heating up the Earth and resulting in the global warming phenomenon [Arrhenius, 1896].

Carbon dioxide (CO_2) is one of the primary atmospheric gases contributing to anthropogenic climate change. Its concentration in the atmosphere has increased by approximately one third since the preindustrial times 1750 [IPCC, 2001] and is now approaching approximately 400 (399.65) parts per million (ppm) [Jones, 2013]. Figure 1 shows the CO_2 levels from 1950 until April 2014 at the Mauna Loa Observatory. The ability of carbon dioxide molecules to absorb and re-emit infrared radiation [Tyndall, 1861] makes it an effective heat-trapping greenhouse gas. Fossil fuel combustion [Keeling, 1973] is one of the primary sources of CO_2 [Mao & Kawa, 2004]. Approximately 57% of anthropogenic carbon dioxide emission is released from fossil fuel use and 17% from deforestation and decay of biomass [IPCC, 2007].

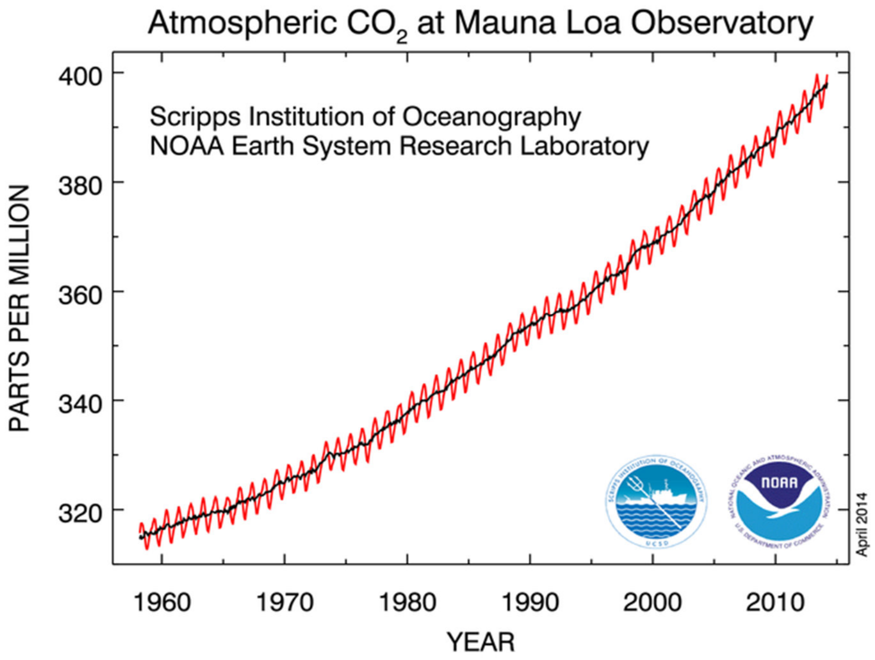

Figure 1: Concentration of $\mathbf{CO_2}$ is approaching 400 ppm for the first time in history. Mauna Loa Observatory, Hawaii: [http://www.esrl.noaa.gov/]

Space-based carbon dioxide (CO_2) measurements to monitor global and regional carbon cycles are of significant importance. The Argus 1000 micro-spectrometer developed at York University, Canada in association with Thoth Technology Inc. is a part of the Canadian Advanced Nano-space eXperiment-2 (CanX-2) satellite's payload [Sarda et al., 2006] launched in 2008. CanX-2 orbits in a low Earth orbit (LEO), 640 km above the Earth's surface where Argus's field of view (FOV) provides a spatial resolution of

1.5 km. The Argus 1000 micro-spectrometer operates in the near infra-red (NIR) region from 1 to 1.7 μm (1000 to 1700 nm) with spectral resolution of 6 nm [Argus Manual, 2010]. An analysis of the spectra it records can provide information about the absorption of infrared radiation by some greenhouse gases (GHGs) such as water vapour (H_2O), carbon dioxide (CO_2), methane (CH_4), and oxygen (O_2). The Argus instrument team has been awarded the Alouette award 2010 in recognition of its contribution to the CanX-2. Figure 2 shows Argus 1000 micro-spectrometer set for space variation test.

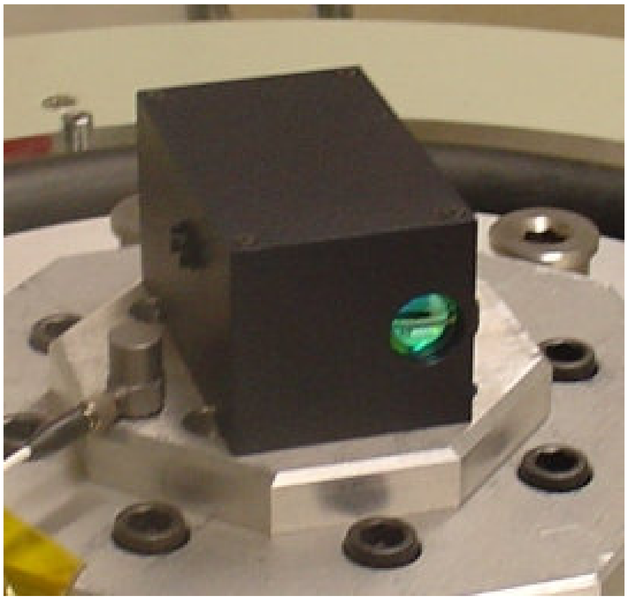

Figure 2: Argus 1000 in the space facility at York University [http://www.thoth.ca/]

1.1 Thesis Statement

The aim of this thesis is to perform a sensitivity analysis for the perturbation of CO_2 in the atmospheric boundary layer (ABL) and the whole atmospheric column. This sensitivity analysis analyzes the absorption of reflected sunlight by carbon dioxide CO_2 at the band 1.58 μm. The sensitivity of back-to-space radiance is then investigated with respect to perturbation of the whole atmospheric column CO_2 (from sea level to 50 km) and the atmospheric boundary layer (from sea level to 2 km). The analysis uses GENSPECT, a line-by-line radiative transfer code that is also used to read and analyze Argus 1000 spectrometer data. To model CO_2 fluctuations, the CO_2 mixing ratio (parts per million) is increased by 1% in the atmospheric boundary layer. Solar zenith angles (SZA) of 30° and 80° are consecutively modeled and back-to-space radiances are plotted. Two possible scenarios of solar radiation paths are assumed. In scenario one, the solar radiation path is assumed to be direct while it is assumed to have multiple reflections from cloud in scenario two. The total back-to-space radiance monitored by the sensor is then calculated in both scenarios. The effect of clouds on solar radiation and CO_2 absorption is explored, analyzed and supported by analysis of Argus 1000 spectrometer data.

1.2 Thesis Outline

The thesis is organized as follows. Chapter 1 describes the sensitivity analysis by providing an introduction to the importance and objectives of the Argus instrument. Chapter 2 provides a literature review on other greenhouse gases measurements from space and sensitivity studies for space-based measurements of atmospheric total column CO_2. This chapter also details the CanX-2 mission to space as well as the internal structure, detector system, optical design, and the operation of the Argus 1000 spectrometer.

Chapter 3 introduces the sensitivity analysis methodology that is adopted in this thesis. It also describes GENSPECT, the radiative transfer model being used and utilized in this analysis to read and analyze Argus 1000 spectrometer data. The radiative transfer equations are discussed in this chapter as well.

Chapter 4 discusses the results of the back-to-space sensitivity to CO_2 absorption at different solar zenith angles in the atmospheric boundary layer and the whole atmospheric column. It examines the solar zenith angles (SZAs) variation effect on the simulated back-to-space radiance. Argus 1000 spectrometer performance is also discussed in this chapter in terms of its current signal-to-noise ratio (SNR). The laboratory experiment setup and results of Argus 100 SNR are described in this chapter as well. The two assumed scenarios of the solar radiation paths, reflected off ground and off cloud, are explored in this chapter. It explores the effect of clouds on the solar radiation and the CO_2 absorption.

Lastly, Chapter 5 provides a conclusion by summarizing the results of the sensitivity analysis of back-to-space radiances to the changes of CO_2 in the boundary layer and outlines the future work that could be performed to improve the current sensitivity method being adopted in this thesis. It also summarizes the Argus 1000 performance in terms of its SNR and the effect of the presence and absence of clouds on the CO_2 absorption at 1.58 µm.

2.0 Background

The Earth's atmosphere can be segmented into upper and lower regions. The lower atmospheric region extends from sea level to an altitude of approximately 50 kilometers (km) [Finlayson & Pitts, 1986] and is the region where some greenhouse gases are found. Greenhouse gases (GHGs) keep Earth warm and habitable for humans. However, an increase of their emissions from anthropogenic activities in the atmosphere will cause the largest positive (warming) forcing [Hansen & Sato, 2004] and lead to some changes, for example, in the atmosphere [WRI, 2014] where more outgoing terrestrial radiation is trapped and heats up the atmosphere.

Radiative Forcing (RF) is an analysis used to determine the effects that greenhouse gases, aerosols, and clouds have on climate change. The combined anthropogenic RF, from 1750 to 2005, is estimated to be +1.6 [–1.0, +0.8] Wm^{-2}, indicating that, since 1750, it is likely that humans have exerted a substantial warming influence on climate [Forster *et al.*, 2007]. Fourth Assessment Report of the IPCC [IPCC 2007, Chapter 2] suggests that the combined anthropogenic RF is likely to be at least five times greater than that due to solar irradiance changes. Table 1 indicates major greenhouse gas concentrations in 2005, their growth rate from 1995 to 2005, and their radiative forcing (RF). The forcing rate of CO_2 is the largest change observed or inferred for any decade in at least the last 200 years [IPCC, 2007]. Comparison between major GHG abundances and radiative forcing is presented below in Table 2 and it is clearly seen that the concentration and forcing values of the mentioned GHGs have increased with time [IPCC 2014, Chapter 8]. Concentration values of the GHGs in Table 2 are illustrated in Figure 3 as a bar chart.

Table 1: Major greenhouse gas content in the air, growth rate for 1995 to 2005 decade and radiative forcing [IPCC 2007, Chapter 2].

Gas	Global Mean Concentration in 2005	Growth Rate 1995 to 2005 (ppm/ppb yr^{-1})	Contributed Radiative Forcing (RF)
CO_2	379 ppm	1.9 ppm yr^{-1}	+1.66 [±0.17] W m^{-2}
CH_4	1774 ppb	~ 0.5 ppb yr^{-1}	+0.48 [±0.05] W m^{-2}
N_2O	319 ppb	0.26 ppb yr^{-1}	+0.16 [±0.02] W m^{-2}

Table 2: Concentration and Radiative forcing values of GHGs in 2005 and 2011 [IPCC 2014, Chapter 8].

	Concentrations		Radiative forcing (Wm^{-2})	
Species / Year	2011	2005	2011	2005
CO_2 (ppm)	391 ± 0.2	379	1.82 ± 0.19	1.66
CH_4 (ppb)	1803 ± 2	1774	0.48 ± 0.05	0.47
N_2O (ppb)	324 ± 0.1	319	0.17 ± 0.03	0.16

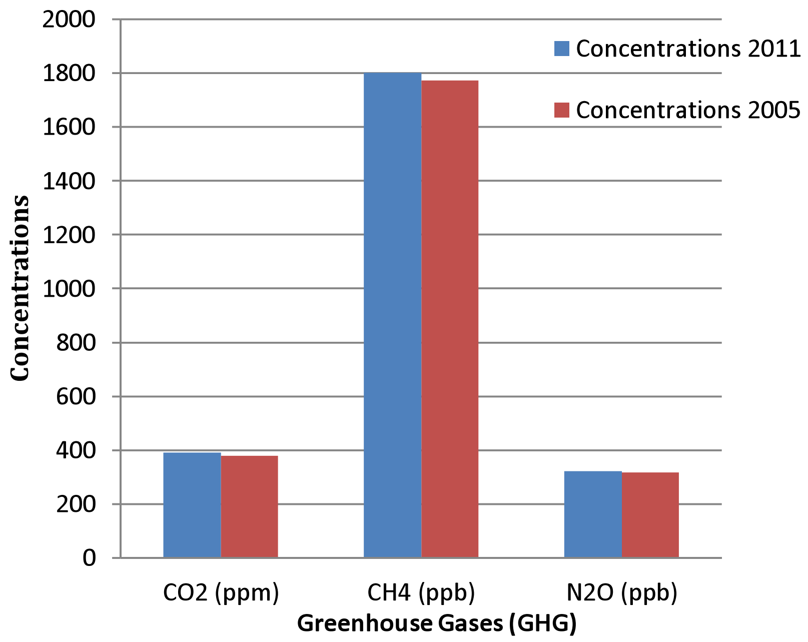

Figure 3: Comparison between GHGs concentration in 2005 and 2011 according to IPCC 2014 data.

Accurate measurements of atmospheric carbon dioxide and other species can provide an objective basis for evaluating reported emissions at regional to continental scales (10^4–10^6 km^2) [Andrews *et al*., 2013]. Precise measurements of atmospheric CO_2 from a global network of surface stations show that fossil fuel combustion, deforestation, and other human activities emissions are superimposed on an active carbon cycle, driven by natural processes in the land biosphere and oceans[Miller, 2011]. However, knowledge of the nature and location of CO_2 sources and sinks, as well as the processes that will affect their future evolution, continues to be limited by a lack of high-precision global measurements of atmospheric CO_2 [Boland *et al*., 2009]. Space-based remote sensing measurements of atmospheric CO_2 have the feasibility to overcome the CO_2 ground measurement limitations in terms of the coverage or resolution to map sources and sinks on regional scales over the globe provided the satellite measurements have sufficiently high sensitivity to the planetary boundary layer (PBL) [Rayner & O'Brien, 2001; Houweling *et al*., 2004; Miller *et al*., 2007;

Chevallier *et al*., 2007; Baker *et al*., 2010; Br´eon & Ciais, 2010]. Figure 4 illustrates different remote sensing platforms and their monitoring capabilities. Several sensitivity studies have evaluated the improvement in carbon flux inversions that would be provided by precise, global space-based column CO_2 data [Dufour & Breon, 2003; Houweling *et al*., 2004; Mao & Kawa, 2004; O'Brien & Rayner, 2002; Rayner *et al*., 2002; Rayner & O'Brien, 2001; Baker *et al*., 2006b]. The consensus of these studies is that satellite measurements with bias-free precisions in the range of 1–10 ppm (0.3–3.0%) will reduce uncertainties in CO_2 sources and sinks due to uniform and dense global sampling [Miller *et al*., 2007].

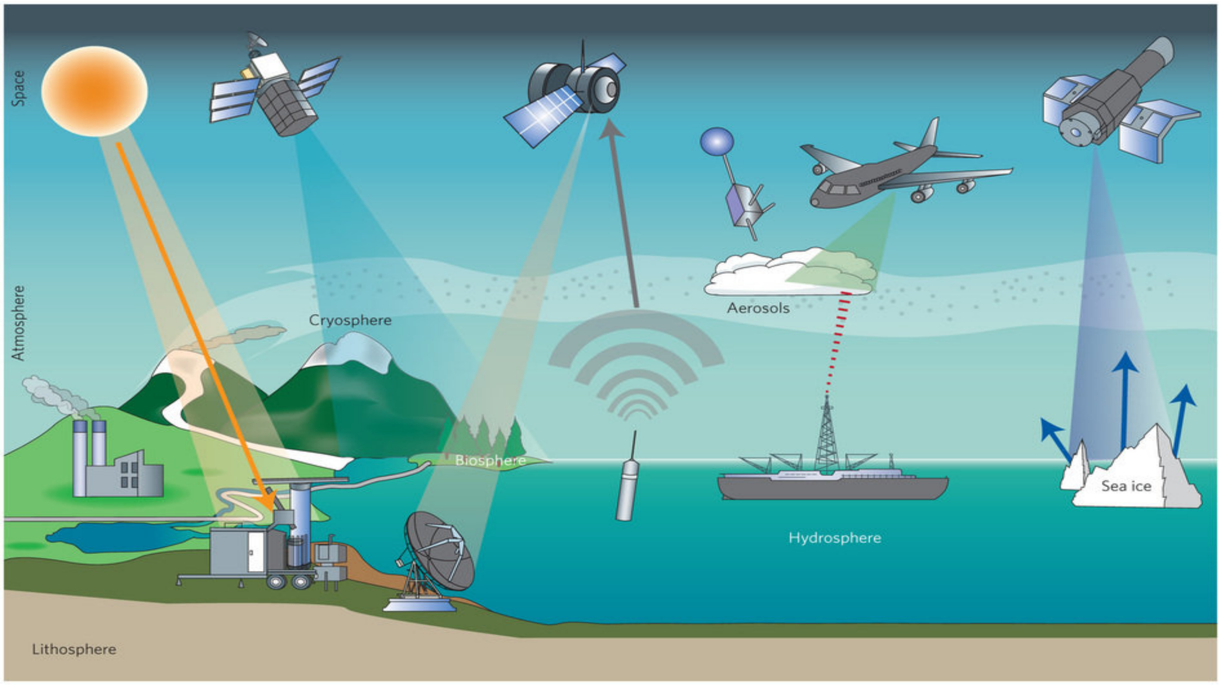

Figure 4: Satellite remote sensing is capable of providing more frequent and repetitive coverage over a large area than other observational means. Figure courtesy of R. He, Hainan University

2.1 Other Greenhouse Gas Measurements from Space

Carbon dioxide (CO_2) is one of the radiative forcing agents [IPCC, 2001] and is one of the most significant anthropogenic greenhouse gases [Warneke *et al.*, 2010]. Carbon dioxide (CO_2) measurements from ground stations are accurate; however; they are sparsely distributed globally, hence, space-based remote sensing instruments with precision required are needed to reduce this uncertainty and provide global coverage of CO_2 sources and sinks. Presently, there are several instruments in space capable of detecting atmospheric carbon dioxide (CO_2) in a wide spectral range. Some of these space instruments operate in the thermal infrared (TIR) range of the spectrum, other instruments detect in the near infrared (NIR)/shortwave infrared (SWIR) interval, while some other instruments cover both SWIR/NIR and TIR regions. Thermal infrared nadir greenhouse gas observations are relatively insensitive to the lower troposphere, due to the lack of thermal contrast. However, many of the sources and sinks of the GHG are located in the boundary layer; therefore, the measurements of the mixing ratios of these gases resulting from regional sources and sinks are most significant in the lower troposphere.

The Infrared Atmospheric Sounding Interferometer (IASI) was launched onboard the MetOp-A platform on October 19th, 2006 in Polar sun-synchronous orbit with an altitude of 817 km above sea level. The detectors that are used in this instrument cover the spectral range that extends from 645 to 2760 cm^{-1} (3.62 to 15.5 μm) in order to resolve CO_2, N_2O, CH_4, and HNO_3 with a vertical resolution of approximately 1%. The design of IASI resulted from a trade-off between the meteorology and atmospheric chemistry requirements [Clerbaux *et al.*, 2009]. The prime objective of the MetOp mission is to obtain continuous, long-term data sets to support global climate monitoring and other environmental forecasting. The Atmospheric Infra-Red Sounder (AIRS) is one of the six instruments [NASA, 2008] that was launched onboard the AQUA platform on May 4, 2002 along with the Advanced Microwave Sounder Unit (AMSU-A) and HSB (Humidity Sounder for Brazil) instruments to provide daily near-global coverage both day and night [Bréon & Ciais, 2010] in the spectral range from 3.7 to 15.4 µm from the normal 705.3 km orbit [Aumann & Pagano, 1994]. The primary objective of AIRS is meteorology with the retrieval of temperature and water vapour profiles. Carbon dioxide ($\mathrm{CO_2}$) retrievals from instruments such as IASI and AIRS in the TIR range will be used to identify errors in the transport models rather than to constrain sources and sinks [Bréon & Ciais, 2010]. AMSU-A operates between 23 and 89 GHz to obtain accurate temperature and moisture profiles in the presence of clouds [Aumann *et al.*, 2003]. HSB is a four-channel microwave radiometer that makes measurements from 150 to 190 GHz with nadir spatial resolution of 16 km.

The High Resolution Infrared Radiation Sounder (HIRS) was launched onboard the National Oceanic and Atmospheric Administration (NOAA) polar-orbiting satellite series in late 1987 to assess long-term variability of the atmospheric properties such as relative humidity in the upper-troposphere layer and temperature and water vapour retrievals [Shi *et al.*, 2008]. HIRS operates in the spectral range 3.8 – 15 µm from an altitude of 833 km [Garand *et al.*, 2001] and provides $\mathrm{CO_2}$ sensitive measurements in the thermal infrared (TIR) spectral range [Cao *et al.*, 2005]. Table 3 shows comparisons between IASI, AIRS and HIRS instruments.

Table 3: Comparison between some selected parameters of the TIR instruments IASI, AIRS and HIRS [Clerbaux *et al*., 2009; Bréon & Ciais, 2010;Garand *et al*., 2001].

Instrument	**IASI**	**AIRS**	**HIRS**
Spectral range	3.62 to 15.5 µm	3.7 to 15.4 µm	3.8 to 15 µm
Resolution	Vertical resolution of approximately 1 km	Spatial resolution 13.5 km (wavelength-dependent)	Spatial resolution at nadir (Earth facing) of 20.3 km and 18.9 km, respectively
Altitude	817 km	705.3 km.	833 km
Platform	MetOp-A	AQUA	MetOp-A and B, and NOAA-N
Launch date	October 19, 2006	May 4, 2002	Late 1987
Purpose	Meteorology, environmental forecasting and global climate monitoring	Meteorology with the retrieval of temperature and water vapour profiles	Long-term variability assessment of the atmospheric properties
Swath	± 48.3°	±49.5	± 49.5
FOV	3.33° x 3.33°	1.1° circular	1.4°

The Scanning Imaging Absorption Spectrometer for Atmospheric Chartography (SCIAMACHY) [Skupin, 2005] was launched onboard the ENVISAT spacecraft on February 28th, 2002 to monitor greenhouse gases such as O_3, H_2O, CO_2, CH_4, NO_2, and CFC's. SCIAMACHY exploits the sunlight transmitted, reflected, and scattered by the Earth's atmosphere or surface in the ultraviolet, visible, and near infrared wavelength interval from 240 to 2380 nm at moderate spectral resolution (0.2 nm – 1.5 nm) and high radiometric accuracy (relative < 1%, absolute < 2–4%) [Bovensmann *et al*., 1999]. ENVISAT (the SCIAMACHY host spacecraft) flies in a polar, sun-synchronous orbit that produces identical light conditions whenever crossing the equator. The primary objective of SCIAMACHY is to determine the concentration and distribution of a large number of atmospheric trace constituents by measuring the radiance backscattered from the Earth in limb and nadir geometry [Skupin, 2005]. Due to its infrared nadir observation capability, SCIAMACHY is the first satellite instrument that is sensitive to CO_2 in the low-troposphere region where most variation occurs [Buchwitz *et al.*, 2005].

The Thermal And Near infrared Sensor for carbon Observation Fourier-Transform Spectrometer (TANSO-FTS) was launched onboard the Greenhouse gases Observing SATellite (GOSAT) on January 23rd, 2009 to detect the near infrared radiation reflected from the earth's surface as well as the thermal infrared (TIR) emitted from the ground and the atmosphere in order to monitor carbon dioxide (CO_2) and the methane (CH_4) globally from 666 km orbit [Kuze *et al.*, 2006]. It is a joint project of Japan’s Aerospace Exploration Agency (JAXA), the Ministry of Environment (MOE), and National Institute for Environmental Studies (NIES) [Yokota *et al.*, 2004]. TANSO-FTS covers the spectral range from 0.76 to 15μm and monitors CO_2 and CH_4 in the spectral regions 1.6 μm and 2.0 μm. An oxygen A-band near the 0.76 μm region is also measured to monitor air mass and to identify cloud effects [Yokota *et al.*, 2004]. SCIAMACHY is able to observe the whole Earth as it has an orbital period of about 100 minutes. Global coverage at the equator is established within 6 days when using the alternating limb/nadir scan option. However, global coverage can be achieved within 3 days (for the 960 km swath width) when only nadir or limb modes are employed [Nett *et al.*, 2001].

The GOMOS (Global Ozone Monitoring by Occultation of Stars) instrument was launched March 1st, 2002 on board the European Space Agency's Envisat satellite to measure O_3, NO_2 , NO_3, neutral density, aerosols, H_2O, and O_2, in the stratosphere and mesosphere by detecting absorption of starlight in ultraviolet (UV), visible (VIS), and near infrared (NIR) wavelengths [Kyrölä *et al.*, 2004]. GOMOS operates in the ultraviolet- visible wavelengths

250–690 nm and two channels are in the near- infrared at 750–776 nm and at 916–956 nm from an altitude of 800 km with spectral resolution of 0.6 nm in a polar, sun-synchronous orbit [Bracher *et al.*, 2005]. The primary goal of GOMOS is to accurately detect the stratospheric ozone, allowing one to monitor global trends in this species over long periods [Nett *et al.*, 2001]. Bertaux *et al.* [2009] provide detailed information about the GOMOS instrument and its specifications. Table 4 compares the main differences between SCIAMACHY, TANSO, and GOMOS instruments.

Table 4: Characteristics of SCIAMACHY, TANSO and GOMOS instruments

Instrument	**SCIAMACHY**	**TANSO**	**GOMOS**
Platform	ENVISAT	GOSAT	ENVISAT
Orbit	sun-synchronous	sun-synchronous	sun-synchronous
Altitude	799.8 km	666 km	800 km
Launched date	March 1st, 2002	January 23rd , 2009	March 1st, 2002
Spectral range	240 to 2380 nm	0.76 to 15μm	250 to 950 nm
Spectral Resolution	0.2 nm–1.5 nm	0.2 cm^{-1}	1.2 nm in UVVIS 0.2 nm in NIR
Viewing Geometry	Nadir, Limb, and solar occultation	Nadir	Occultation mode and monitoring modes (uniformity, spatial spread and linearity mode)
Scientific Objective	Provides global measurement of various trace gases in the troposphere and stratosphere	To estimate emissions and absorptions of the greenhouse gases on a sub-continental scale	Observation of ozone in the stratosphere and the monitoring of trends.
Total Mass	215 kg	250 kg	175 kg
Power	175 W	310 W	200 W
Field of View	0.045° x 1.8°	cross-tr. ±35° along-tr. ±20°	0.6°
Volume	1.8×0.9×1.0 m^3	1.2×1.1×0.7 m^3	30 cm × 20 cm

The Michelson Interferometer for Passive Atmospheric Sounding (MIPAS) is a Fourier transform spectrometer designed for measurement of trace species from space [Clarmann *et al.*, 2003]. MIPAS was launched on March 1st, 2002 onboard the Envisat spacecraft into a polar sun-synchronous orbit. With a high spectral resolution (0.035 cm^{-1}) and covering the mid-infrared from 4.1 to 14.7 nm (685–2410 cm^{-1}), the opportunity to understand and study active odd nitrogen species NO and NO_2, from their emissions at 5.3 and 6.2 µm respectively [Funke *et al.*, 2005] is present. The Thermal Infrared Sensor (TIRS) was launched onboard LANDSAT-8 on February 11th, 2013 with two spectral bands: Band 10 TIRS 1 (10.6–11.19 µm) and Band 11 TIRS 2 (11.5–12.51 µm) both with spatial resolution 100 m. The Global Ozone Monitoring Experiment (GOME) was launched in April 1995 aboard the European Space Agency's (ESA) Second European Remote Sensing Satellite (ERS-2) and measures the reflected and scattered sunlight from the Earth's atmosphere and surface in nadir viewing mode in the spectral region 240–790 nm at a moderate spectral resolution of between 0.2 and 0.4 nm. The primary objective of the GOME mission is to quantify the global distribution of ozone and some other trace gases such as O_3, O_4, NO_2, BrO, NO_3, H_2O, and O_2 [Burrows *et al.*, 1999]. The Atmospheric Chemistry Experiment (ACE) is a Canadian-led satellite mission that was launched on Aug 12th, 2003 [Bernath *et al.*, 2005] to measure the concentrations of more than 30 atmospheric constituents by absorption of sunlight. However, the main objective of ACE is to make measurements that will improve understanding of the chemical and dynamical processes that control the distribution of ozone in the upper troposphere and stratosphere [Bernath, 2006]. ACE covers the spectral interval from 2.2 to 13.3 µm.

The Moderate-resolution Imaging Spectroradiometer (MODIS) onboard the Terra (EOS AM) and Aqua (EOS PM) satellites was launched on December 18th, 1999 and May 4th, 2002 respectively, to measure Earth’s radiance in 36 bands, ranging from 0.4 to 14 µm [Savtchenko *et al.*, 2003] at varying spatial resolutions 2 bands at 250 m, 5 bands at 500 m, and 29 bands at 1 km. Its objective is to provide large-scale global measurements including changes in radiation budget, Earth's cloud cover, and processes occurring in the oceans, on land, and in the lower atmosphere. The Advanced Very High Resolution Radiometer (AVHRR) was first launched on October 1978 onboard TIROS-N (Television Infrared Observation Satellite) with a 4-channel radiometer that was subsequently improved to a 5-channel instrument (AVHRR/2) that was initially carried on NOAA-7 (launched June 1981). The latest instrument version is AVHRR/3, with 6 channels, first carried on NOAA-15 launched in May 1998 [NOAA, 2013]. The main objective of the AVHRR scanning radiometer is to remotely determine the cloud cover and the surface temperature of Earth, upper cloud, and/or a body of water such as oceans, seas, and lakes. The AVHRR/3 is a six-channel scanning radiometer providing three solar channels in the visible- near infrared region and three thermal infrared channels as follows: 0.58–0.68 µm (green to orange) for daytime cloud and surface mapping, 0.725–1.10 µm (red to near-infrared) for land-water boundaries, 1.58–1.64 µm (near infrared) for snow and ice detection (off during nighttime), 3.55–3.93 µm (middle infrared) to map night cloud and measure sea surface temperature (off during daytime), 10.30–11.30 µm (thermal infrared) for night cloud mapping and sea surface temperature, and lastly 11.50–12.50 µm (thermal infrared) to measure sea surface temperature.

The Orbiting Carbon Observatory (OCO) [Pollock et al., 2010] was designed to fly in the EOS Afternoon Constellation (A-Train) with a 705 km Sun-synchronous orbit [Bösch *et al*., 2006] and make measurements of carbon dioxide concentrations from space with the precision and accuracy required to identify sources and sinks on regional scales (~1,000 × 1,000 km^2) and to characterize their variability on seasonal timescales [Crisp *et al*., 2004]. Unfortunately, OCO was lost due to a failure of the launch vehicle on 24 February 2009. Since then, work has started on OCO-2 which was launched in July 2014. The OCO instrument is designed to make very high spectral resolution measurements close to 1.6 µm and 2 µm, two spectral bands that show a few narrow CO_2 absorption lines and that are free from other gaseous absorption, and at 0.76 µm that corresponds to an oxygen absorption band. The latter is used for correction of surface pressure and atmospheric scattering [Bréon & Ciais, 2010]. OCO has three viewing strategies: Nadir, Glint and Target. In the Nadir mode, the instrument looks straight towards the local sub-spacecraft point on the Earth‘s surface to gain the highest spatial resolution. In the Glint mode, the instrument boresight points at the spot on the Earth surface where sunlight is specularly reflected. This mode is necessary over the ocean to get a sizeable reflectance from the surface. Finally, the instrument may aim at specific targets and this mode is useful for calibration and validation of the CO_2 products [Bréon & Ciais, 2010]. OCO-2 used the OCO instrument and mission design including the same orbit to minimize the risk and time required to launch readiness. OCO-2’s most critical requirement is to measure the column–averaged dry air mole fraction X_{CO_2} with 1–2 ppm (0.3–0.5%) precision on regional scales (1,000 × 1,000 km^2) at semi-monthly intervals for up to two years. The Field of View (FOV) of OCO-2 was designed to observe the Earth’s surface with an area of 3 km^2 in nadir to maximize the number of cloud-free scenes observed. The two viewing geometry modes Nadir and Glint are planned for alternating 16 day repeat cycles since the spacecraft lacked sufficient pointing agility to switch rapidly between Nadir and Glint modes. It is noteworthy to mention that the Argus 1000 Micro-spectrometer is the predecessor of OCO-2 and it was launched on April 2008 onboard CanX-2 (Canadian Advanced Nanosatellite eXperiment-2). Argus 1000 was designed to measure the greenhouse gases in the atmosphere and it operates in a very narrow spectral range from 1 µm to 1.7 µm with a spectral resolution of 6 nm. A more detailed discussion of the Argus spectrometer is found in Section 2.4. Table 5 shows the technical features of Argus 1000 spectrometer and OCO-2. It is clearly seen, from Table 5, that there are some similarities and differences between Argus 1000 spectrometer and OCO-2. They have the same orbit mode (sun- synchronous), very close spatial resolution, and approximately same orbital altitude (~ 640 km). On the other hand, however, there are some differences between them such as number of instruments, spectral range, spectral resolution, mass, power and volume. OCO-2 carries 3 grating spectrometers where each spectrometer has only one band in a specific range on the electromagnetic spectrum (O_2 A-band, CO_2 weak and strong bands in the NIR) while CanX-2's Argus 1000 is only one grating spectrometer operating in the NIR spectral range (1000 to 1700 nm).

Table 5: OCO-2 and Argus main technical specifications

Instrument	**OCO-2**	**Argus 1000**
Platform	**LEOStar-2**	**CanX-2**
Orbit	sun-synchronous	sun-synchronous
Altitude	686 km	644 km
Launched date	01 Jul 2014	28 April 2008
Instrument	3 Grating Spectrometers	1 Grating Spectrometer
Spectral range	O_2 A-Band: 0.758 to 0.772 μm Weak CO_2: 1.594 to 1.619 μm Strong CO_2: 2.042 to 2.082 μm	1.0 – 1.7 μm
Spectral Resolution	O_2= 17500 $(\lambda\backslash\Delta\lambda)$ CO_2= 20000 $(\lambda\backslash\Delta\lambda)$ or 0.01 cm^{-1}	6 nm or 283 $(\lambda\backslash\Delta\lambda)$ at 1700 nm
Spatial Resolution	$< 3\ km^2$	$\sim 2.8\ km^2$
Viewing Geometry	Nadir, Glint and Target-tracking	Nadir
Scientific Objective	To provide space-based measurements of CO_2 with precision and accuracy needed.	To measure greenhouse gases in the atmosphere such as CO_2, H_2O, O_2 and CH_4
Mass	140 kg, total 450 kg (with the bus)	>230 g total 3.5 kg (with the bus)
Power	105 W	2.3 W
IFoV (along × across-track)	2.25 x 1.29 km at Nadir	1.4 x 1.4 km at Nadir
FOV	2.9 km^2 /1.8 mRad / 0.10º	3 km^2 / 2.18 mRad / 0.15º
Swath	10.4 km at Nadir or 0.8º	-
Volume	1600 × 400 × 600 mm3	45 × 50 × 80 mm3
Approximate Cost	$465 million	$1 million

Thermal-IR instruments such as AIRS, TES, and IASI measure CO_2 above the mid-troposphere; however, the lack of sensitivity of these thermal-IR data to near-surface CO_2 and potential shortcomings in the description of vertical transport in transport models result in a limited value of these observations for inverse studies of surface fluxes [Chevallier *et al*., 2005].

TIR instruments directly measure the greenhouse forcing by CO_2 in the present climate. In contrast, solar NIR instruments such as Argus 1000, GOSAT, and OCO-2 measure the total CO_2 column and therefore provide the highest sensitivity to the surface fluxes. NIR instruments provide insight needed to predict future rates of CO_2 buildup and climate impacts. Combining solar NIR and thermal IR measurements could provide insight into vertical atmospheric transport of CO_2.

2.2 Sensitivity Studies for Space-Based Measurements of Atmospheric Total Column CO_2

Carbon dioxide levels are monitored and measured accurately by hundreds of ground stations in 66 countries around the globe. However, the majority of these stations are located in the Northern Hemisphere while there are few stations in the Southern Hemisphere, which makes their dataset limited for global studies. Uncertainty in the global carbon budget estimate based on the scattered ground stations is approximately 8.8 Gigatonnes of carbon dioxide per year ($GtCO_2$/y) which is equal to about 1 ppm/year [Rayner & O'Brien, 2001]. Atmospheric CO_2 measurements from space with high spatial resolution are of great assistance and significance for global and regional carbon-cycle studies. In the past two decades, some studies such as [Aoki, *et al.*, 1993; J. Park, 1997; and Tolton & Plouffe, 2001] have investigated the possibility of monitoring atmospheric total column CO_2 from space. Recent studies such as [Mao & Kawa, 2004, Dufour & Bréon, 2003, O'Brien & Rayner, 2002, Rayner & O'Brien, 2001, and Kuang *et al.*, 2002] have explored and addressed this issue with a similar measurement methodology.

Mao and Kawa [2004] examined several potential CO_2 absorption bands and selected the 1.58 µm band as optimal because the solar flux is higher at this wavelength than at longer wavelengths and because interference from other gas species is minimal. They described some basic radiative features and properties of the 1.58 μm band for a realistic atmosphere with both absorption and scattering. Furthermore, they tested the back-to-space radiances for changes in the atmospheric boundary layer CO_2 amount under different geophysical conditions such as solar zenith angle, cirrus clouds, aerosols, and water vapour. They also addressed the dependence of the radiance sensitivity on the atmospheric temperature and the surface pressure. Rayner and O'Brien [2001] have shown that space-based measurements of the atmospheric total CO_2 column, even with poorer precision (~2 ppmv, 0.5%), would provide a better constraint on the geographic and temporal distributions of CO_2 sources and sinks than the existing surface network. O'Brien and Rayner [2002] measured the solar radiance at two frequencies in the CO_2 absorption band at 1.61 μm, which in principle allows the CO_2 column to be estimated precisely in a clear atmosphere, not in the presence of thin cloud and aerosol. They argued that precision better than a few percent is unlikely, because scattering by cirrus shortens the mean path lengths of photons reflected to space, and hence biases the estimate of the CO_2 column low. Dufour and Bréon [2003] used the differential absorption technique, from high-resolution spectroscopic measurements in the 1.6 μm and 2 μm CO_2 absorption bands to analyze the feasibility of a CO_2–weighted column estimate. They attempted to quantify errors due to the radiometric noise, uncertainties in the temperature, humidity, and surface pressure, spectroscopic coefficients, and atmospheric scattering. Their error analysis shows that there are two major sources of error that need to be resolved for a useful measurement of CO_2 from space. These sources of error are spectroscopic parameters and the impact of atmospheric scattering resulting from aerosol and undetected clouds [Dufour & Bréon, 2003].

Kuang *et al.* [2002] introduced a method that employs high-resolution spectra of reflected sunlight taken simultaneously in near infrared (NIR) CO_2 (1.58 μm and 2.06 μm) and O_2 (0.76 μm) bands to measure the column-averaged CO_2 dry air volume mixing ratio X_{CO_2} from space. Their simulation shows that precisions of ~0.3–2.5 ppmv for X_{CO_2} can be achieved from individual clear sky soundings for a range of atmospheric/surface conditions when the scattering optical depth is less than ~0.3. Their study concluded that the 3-band, high-resolution, spectrometric approach using NIR reflected sunlight has the potential for highly accurate X_{CO_2} measurements.

2.3 CanX-2 Mission to Space (Canadian Advanced Nanosatellite eXperiment-2)

The Canadian Advanced Nanospace eXperiment (CanX-2) is a series of satellites that were launched by the University of Toronto Institute for Aerospace Studies' Space Flight Laboratory (UTIAS/SFL) in September, 2001 [Rankin *et al.*, 2005]. The CanX-2 program was developed to provide Canada with a continuous supply of highly skilled and experienced space system and microsatellite engineers while at the same time providing a low-cost, quick-to-launch satellite platform upon which to execute scientific and technology demonstration missions [Sarda *et al.*, 2006]. CanX-2 is a triple CubeSat measuring 10 × 10 × 34 cm as shown in Figure 5 and is approximately 3 kg in mass, that allows for greater available space for payloads and surface area to push the envelope of what has been previously attempted in this scale of spacecraft [Sarda *et al.*, 2006]. Figure 6 shows the CanX-2 overview bus and positions of its devices and instruments. Figure 7 shows the CanX-2 mission patch.

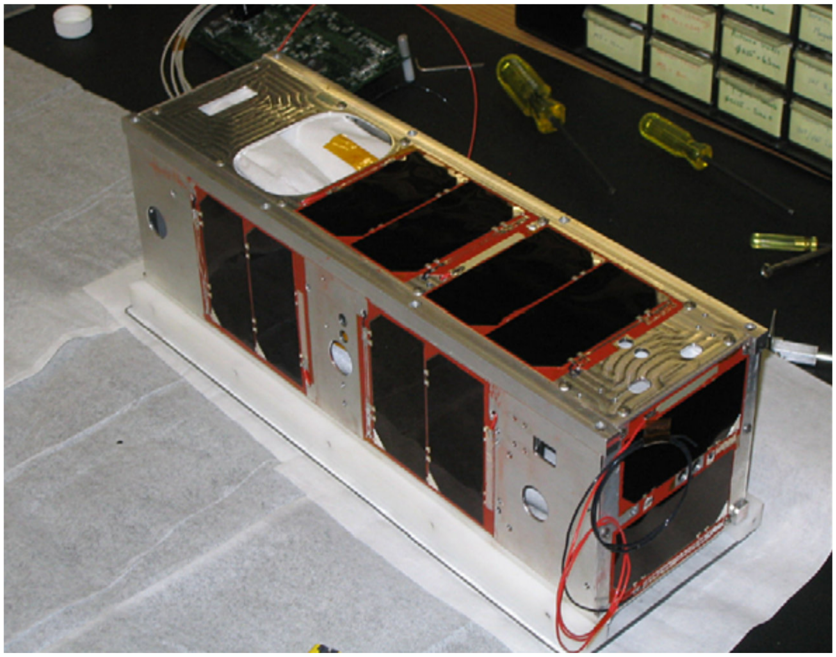

Figure 5: Partly integrated CanX-2 spacecraft [Courtesy: UTIAS]

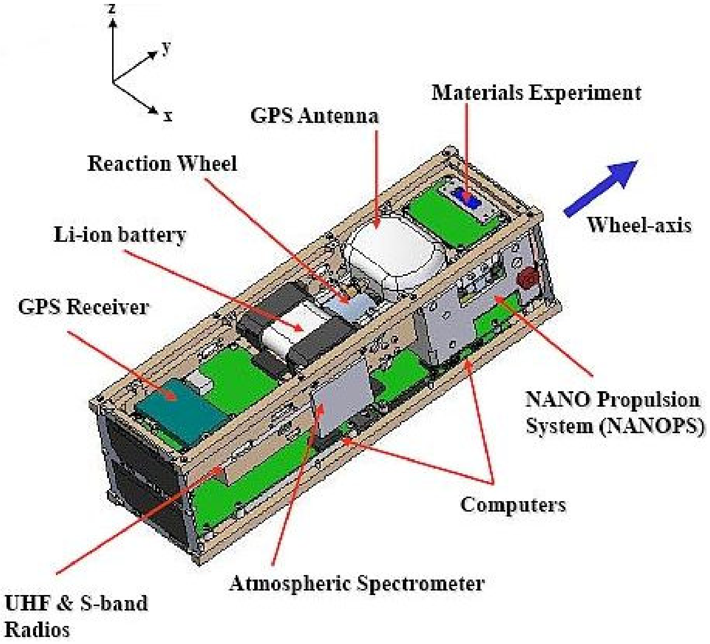

Figure 6: Accommodation of subsystems in the CanX-2 bus [Courtesy: UTIAS]

Figure 7: CanX-2 Mission Patch [Courtesy: UTIAS]

2.3.1 Payloads

CanX-2 hosts several science and engineering experiments, each with the potential and promise of developing and advancing knowledge and understanding within the scientific community. The science payloads are shown in Figure 8. Science instruments aboard CanX-2 include an atmospheric spectrometer (Argus 1000 spectrometer) to measure greenhouse gases (York University), a GPS radio occultation experiment developed by the University of Calgary to characterize the upper atmosphere, and a space materials experiment to evaluate the effects of atomic oxygen on a protective coating (University of Toronto).

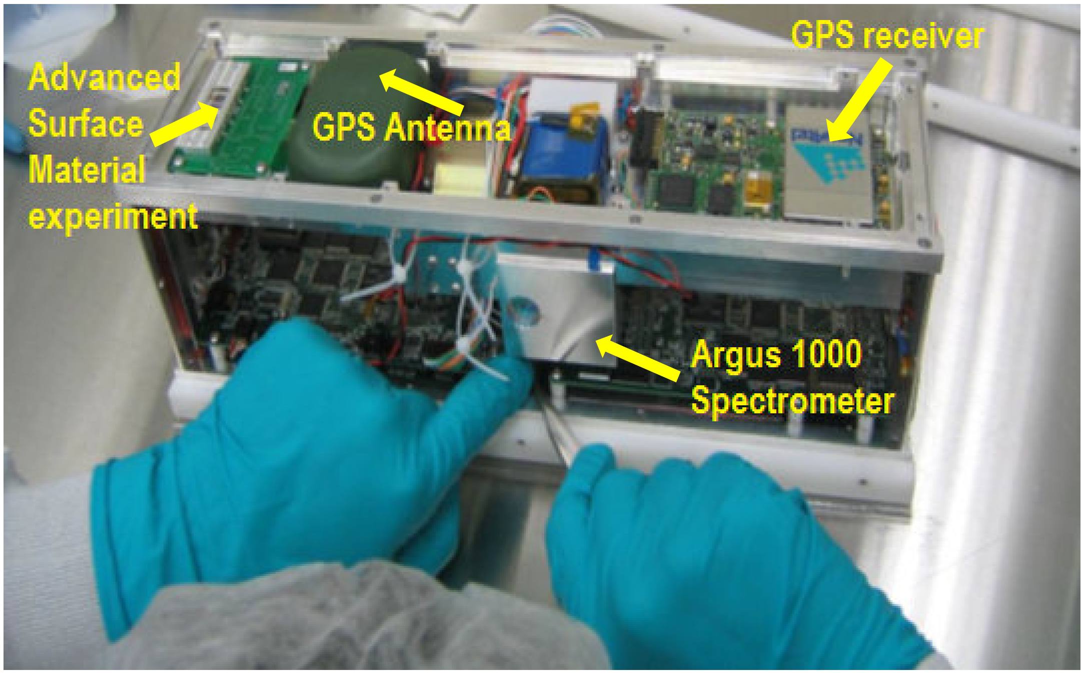

Figure 8: The science payloads. The atmospheric spectrometer, GPS antenna and receiver, and advanced surface material experiment [Courtesy: UTIAS].

2.3.2 Launch of CanX-2 Satellite

The CanX-2 Nanosatellite was launched into a sun-synchronous, near polar, low Earth orbit (LEO) on April 28th, 2008 aboard the Indian Polar Satellite Launch Vehicle (PSLV) from SDSC (Satish Dhawan Space Centre), Sriharikota, India. The shared launch comprised of eight secondary payloads, and CanX-2 included, and the primary payload of a high-resolution panchromatic imaging satellite (CartoSat-2A), developed by the Indian Space Research Organization (ISRO). Figure 9 shows the CanX-2 position in the upper stage of the PSLV-C9 rocket. Figure 10 shows the final stage of PSLV-C9 on the launch pad, India.

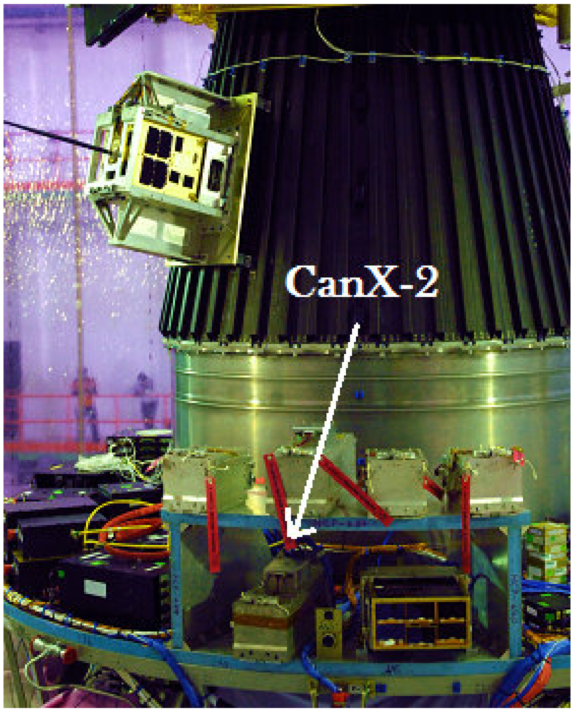

Figure 9: PSLV-C9 upper stage and the position of CanX-2 [Courtesy: ISRO]

Figure 10: (A) PSLV-C9 on its way to the launch pad, (B) PSLV-C9 on the launch pad, April 28th, 2009 [Courtesy: UTIAS/ISRO].

2.4 Argus 1000 Spectrometer

The Argus 1000 micro-spectrometer is a new generation of miniature remote sensing instruments to monitor greenhouse gas emissions from space. The Argus 1000 spectrometer is capable of monitoring ground-based sources and sinks of anthropogenic pollution. The instrument was designed to take nadir observations of reflected sunlight from Earth's surface and atmosphere. The nadir viewing geometry of Argus is of particular utility as this observation mode provides the highest spatial resolution on the bright land surfaces and returns more useable soundings in regions that are partially cloudy or have significant surface topography. Figure 11 illustrates the science of observation mode of the Argus 1000 spectrometer. Signal-to-noise ratios of observations over dark ocean surfaces may not be adequate in Nadir mode. This limitation of Nadir mode might be overcome by employing Glint mode, though the actual glint spot is too bright and would saturate the instrument. Glint mode measurements should be made a few degrees away from the actual glint spot.

Spectra of reflected radiation from the Earth's surface provide some important absorption features that are associated with the absorption of solar radiation by gases in the atmosphere. Measurements of the absorption of reflected sunlight by $\mathrm{CO_2}$ at NIR wavelengths were extremely sensitive to the $\mathrm{CO_2}$ concentration change near the surface, where its sources and sinks are located [Boland *et al*., 2009]. The NIR nadir spectra measured by the Argus 1000 spectrometer contain information on the vertical columns of important atmospheric trace gases such as carbon dioxide ($\mathrm{CO_2}$) and water vapour ($\mathrm{H_2O}$). Other greenhouse gas species such as nitrous oxide ($\mathrm{N_2O}$), hydrogen fluoride (HF), methane ($\mathrm{CH_4}$) and carbon monoxide (CO) have NIR absorption features within the Argus spectral range from 1000 to 1700 nm; however, they are relatively weak [Jagpal, 2012]. Table 6 shows the gas species observed by Argus. The Near infrared (NIR) absorption amount depends on the concentration of absorber gas along the radiation path without the photons being attenuated by some physical process such as scattering or saturation.

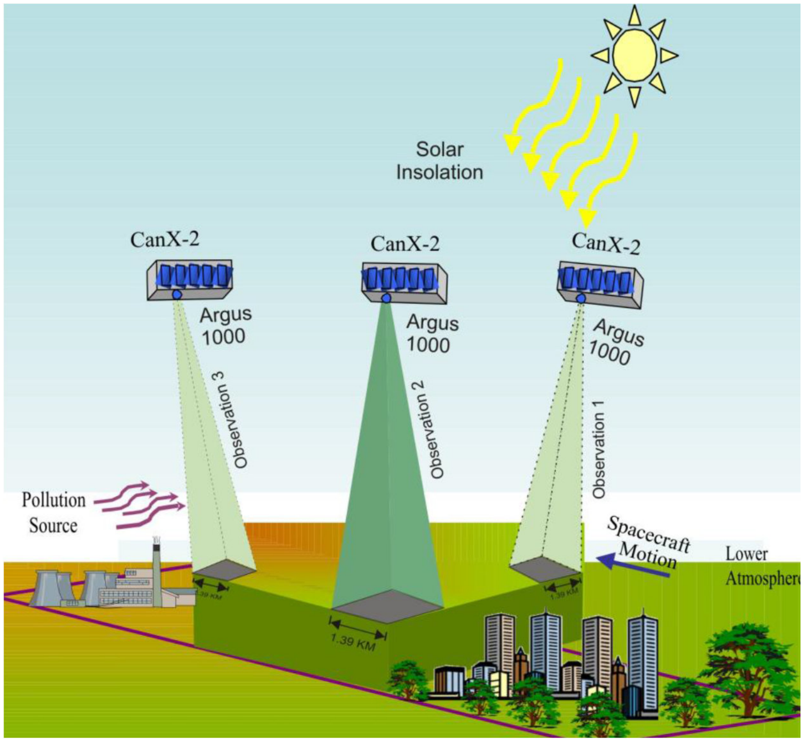

Figure 11: Nadir viewing geometry of Argus 1000 spectrometer. [Image credit: Jagpal, 2012]

Table 6: Gas species observed by IR Argus 1000 spectrometer and their absorption bands.

Observed Target Gas	Absorption wavelength
Carbon Dioxide (CO_2)	1240 nm, 1420 nm, 1570 nm, 1600 nm
Water (H_2O)	900nm, 1200 nm, 1400 nm
Carbon Monoxide (CO)	1630 nm
Methane (CH_4)	1660 nm
Oxygen (O_2)	1260 nm

Optical depth is a quantity of fundamental importance in atmospheric studies [Bodhaine *et al*., 1999] which related to the vertical path from Earth's surface to outer space. Argus 1000 records any changes in optical depth associated with the variation of the atmospheric gas species in the spectral interval 1000–1700 nm. With a spectral resolution of 6 nm and instantaneous field of view (IFOV) 2.18 mRad, the Argus 1000 spectrometer provides a high spatial resolution pollution monitoring capability. Table 7 illustrates the technical specification of the Argus 1000 spectrometer [Argus Manual, 2010]. Before flight, Argus 1000 was successfully calibrated and tested to make sure it met the space environment conditions. The Argus 1000 spectrometer (Figure 12) calibration procedure is detailed by Jagpal, 2012. Geolocation algorithms have been developed by Benari [2012] to locate Argus observations and prepare them for further analysis.

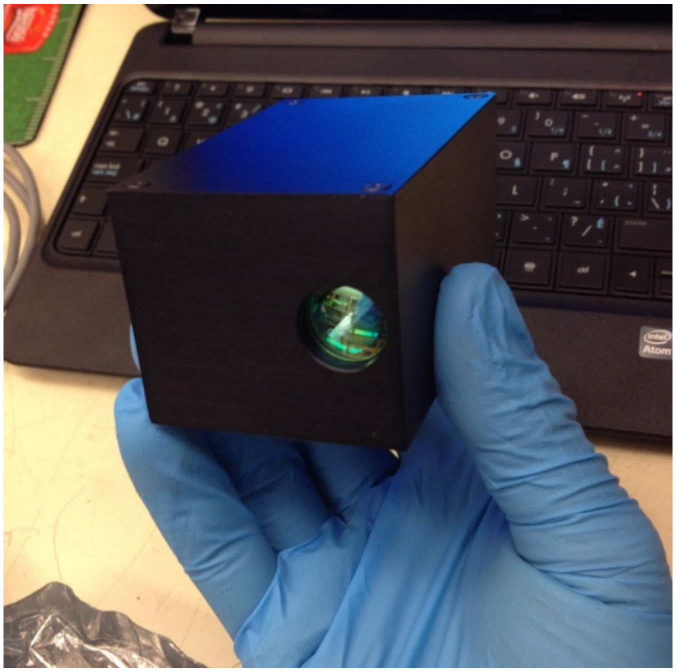

Figure 12: Argus 1000 spectrometer commercial unit shown at the Space Engineering Laboratory, York University.

Table 7: Argus 1000 specifications [Argus manual, 2010].

Argus 1000 parameter	**Value**
Type	Grating spectrometer
Configuration	Single aperture spectrometer
Mass	Less than 230 g
Accommodation	45 mm x 50 mm x 80 mm
Field of View	0.15º viewing angle around centered camera boresight with 15mm fore-optics
Spectral range	900 – 1700 nm
Spectral resolution	6 nm
Spectral Channels	100 (typical)
Spatial resolution	1.25 km
Detector	256 element InGaAs diode arrays with Peltier cooler (100 active channels)
Grating	300 or 600 g/mm
Integration Time	500 μs to 4.096 sec
Operating Temp	–20ºC to +40ºC operating temperature
Survival Temp	–25ºC to + 50ºC survival temperature
Signal to Noise Ratio	~ 700:1
Power	2.3 W

2.4.1 Argus 1000 Spectrometer Design

The Argus 1000 micro-spectrometer weighs less than 230 g, which makes it a very strong candidate for low-mass cost effective space missions. The instrument's dimensions are $45 \times 50 \times 80$ mm^3 as shown in Figure 13. The entrance aperture is on the –X face and its center is located 10 mm from the edge of the +Y side and 22.5 mm from the +Z side. The connector is on the –Y side, with its center 13 mm from the +X face and 5 mm from the –Z face.

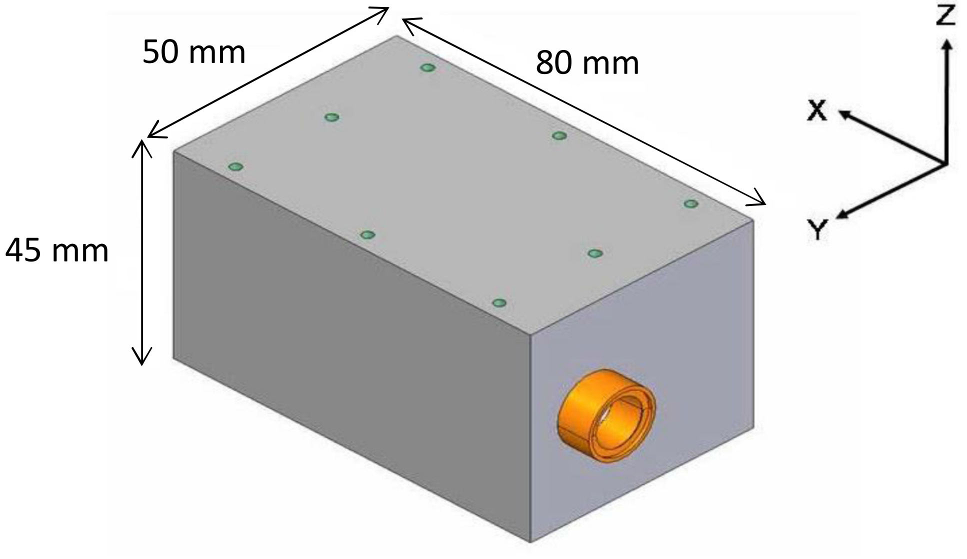

Figure 13: Argus 1000 External Dimensions [Courtesy: Thoth Technology Inc., 2010] .

2.4.2 Detector System

Argus utilizes an indium gallium arsenide ($In_xGa_{1-x}As$) sensor that is a semiconductor with excellent transport and optical properties. The device employs a linear indium gallium arsenide (InGaAs) photodiode array with high-quantum efficiency pixels, as shown in Figure 14, in the infrared to detect the emitted radiation from a distant surface tile that has been divided spectrally by the grating optics. The detector array has a quantum efficiency of approximately 85% in the spectral range between 1000 nm and 1600 nm. The detector array has 1x256 elements and is actively cooled. It is a hybrid InGaAs and CMOS (Complementary metal–oxide–semiconductor) active-pixel readout electronics which buffers, amplifies, and stores the photo-current according to principles shown in Figure 15. The generated photo current is processed by a capacitive transimpedance amplifier (CTIA) into a measurable voltage. There are two values of feedback capacitor may be selected externally (the HIGH setting enhances dynamic range, the LOW setting increases sensitivity). The ADC precision can be enhanced from 10-bits to 13-bit by utilizing the co-adding feature [Argus Manual, 2010].

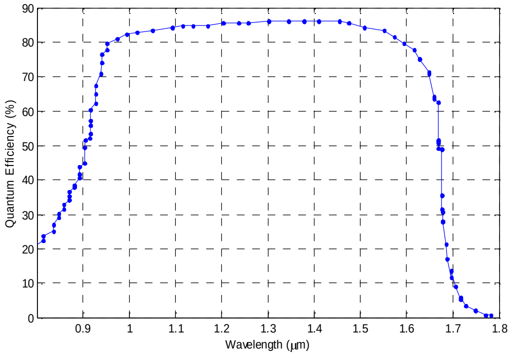

Figure 14: Detector Quantum Efficiency for 1.7 µm device.

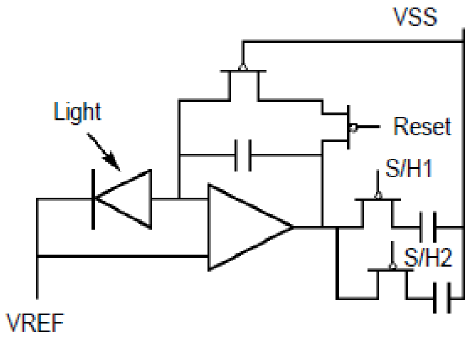

Figure 15: Schematic of an integrating transimpedance amplifier.

2.4.3 Optical Design

The Argus optical system was designed in an innovative way to meet the critical requirements for obtaining accurate and precise data. Such requirements include the optical resolution, spectral range, mass, and size. The spectral range (1000 nm to 1700 nm for standard version or 1700 nm to 2200 nm for extended range version) was chosen to measure both Earth and atmospheric emission in the short wavelength infrared (SWIR) region with a relatively high spectral resolution of approximately 6 nm.

The CanX-2 instrument employs an infrared optical triplet lens in the fore optics to provide an image tile tightly focused on a beam stop that provides the spatial filtering for the device. Other optical filters prevent the visible radiation (that is below 900 nm) from entering the spectrometry chamber. The device employs collimating optics to collimate the reflected radiation from a 1.5-km tile onto a reflective grating that reflects a spectrally divided image onto another mirror (focusing optics) that focuses the first spectral order of the surface tile image onto the detector. Figure 16 shows the internal structure of Argus while Figure 17 illustrates the layout of Argus optical design and Figure 18 shows the instrument's functional design. The diffraction grating is of particular importance in the light dispersion.

The instrument employs a 300 grooves/mm grating, which provides the desired and necessary spectral range (1000 nm to 1700 nm) to observe O_2, CO_2, and H_2O absorption. The Grating plays a key role in determining the resolution of a spectrometer. Increasing the density of the grating grooves (more than 300 g/mm) would enhance the resolution but this would be at the expense of a narrow spectral range.

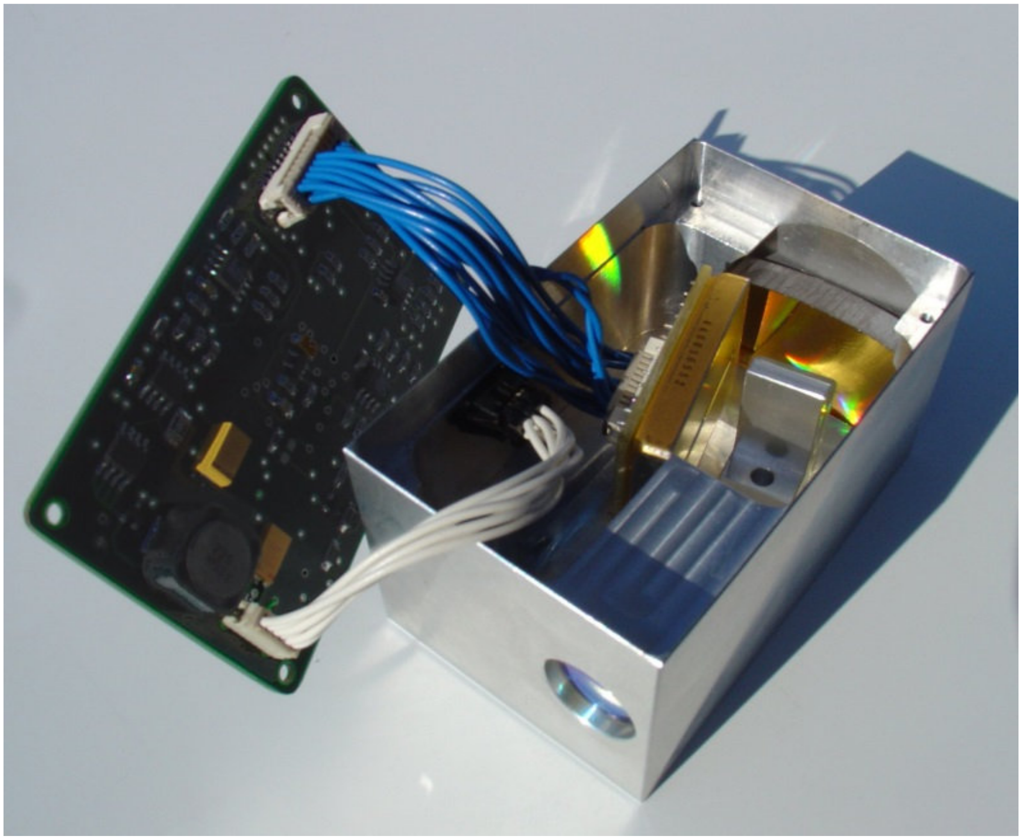

Figure 16: The internal structure of the Argus 1000 spectrometer.

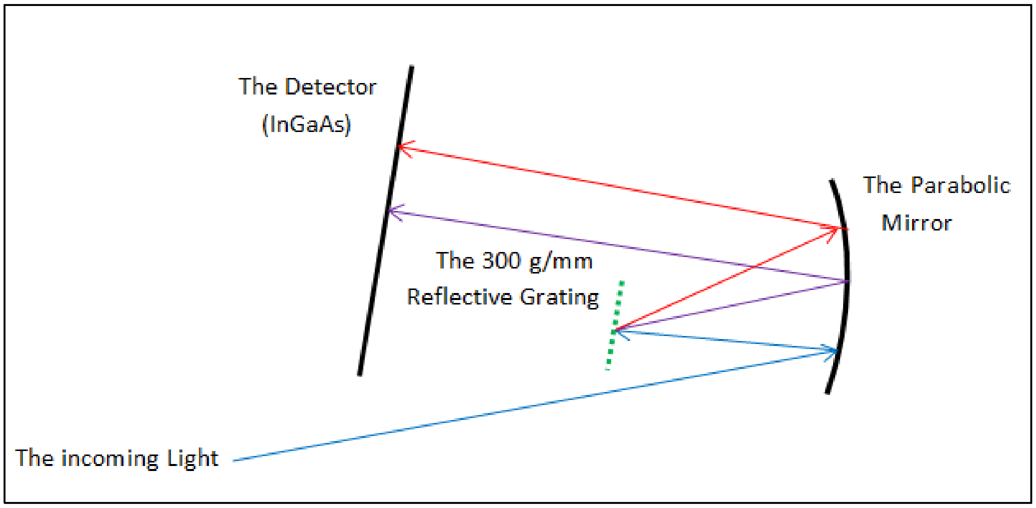

Figure 17: The optical design layout of Argus. The main mirror is 35 mm and the input mirror is 15 mm. The grating is 300 g/mm.

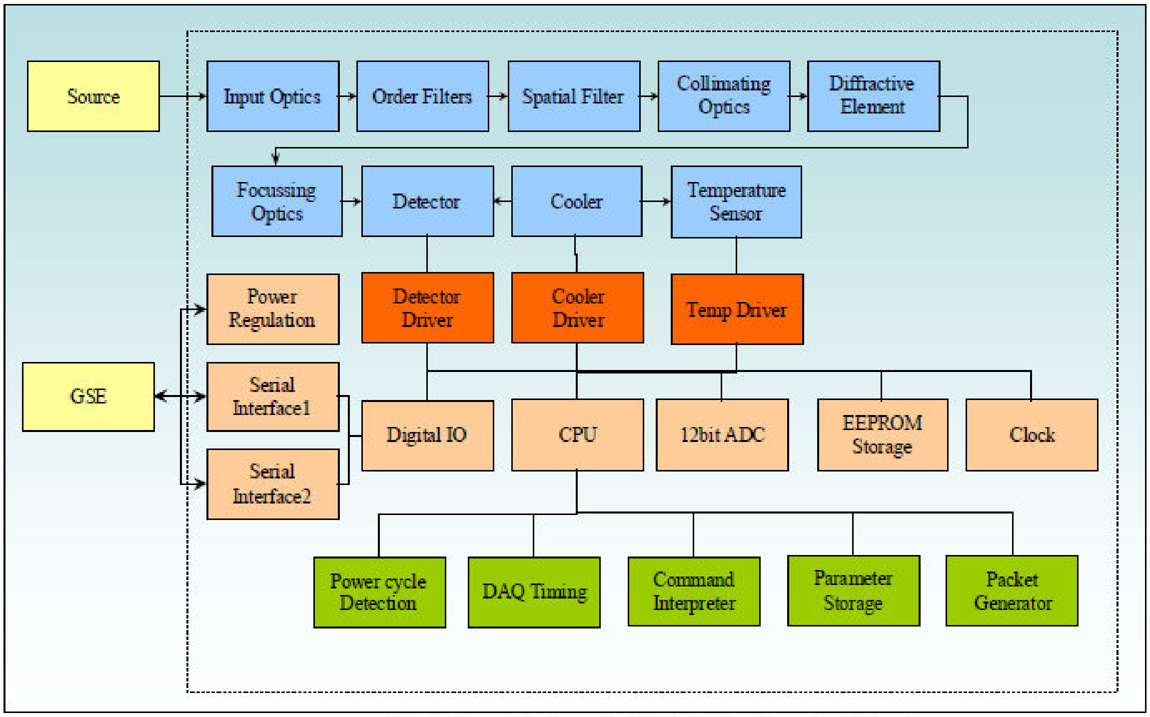

Figure 18: Argus functional diagram showing optics (blue), electronics layer (brown), cooler components layer (red), software layer (green) [Argus Manual, 2010].

2.4.4 Instrument Operation

The Argus 1000 spectrometer team at York University is commanding and controlling the instrument alongside CanX-2 satellite operations and the control unit at UTIAS (University of Toronto Institute for Aerospace Studies). Argus collects data over the determined targets for a four-week long period and stops for a two-month break, allowing the other two experiments aboard CanX-2 to function. The Argus team at the Space Engineering Laboratory at York University prepares the observation tables for the desired targets around the globe using the Systems Tool Kit (STK) software. The Argus-1000 target list contains 35 sites around the Earth as shown in Figure 19. Figure 20 shows some of Argus targets and typical CanX-2 overpasses. STK is used to simulate the passes of the CanX-2 satellite over the selected targets providing a list of start and stop times and the duration time in seconds for each pass every week during the observation campaign. Table 8 shows a sample of the typical observation table generated by STK. The highlighted pass in Table 8 is an indication for the operations team at UTIAS to prioritize it in this campaign. The generated lists of Argus targets are sent to the operations unit at UTIAS to start the observation week. The operations team at UTIAS will then send the collected data to the Argus team at York University for processing and analysis.

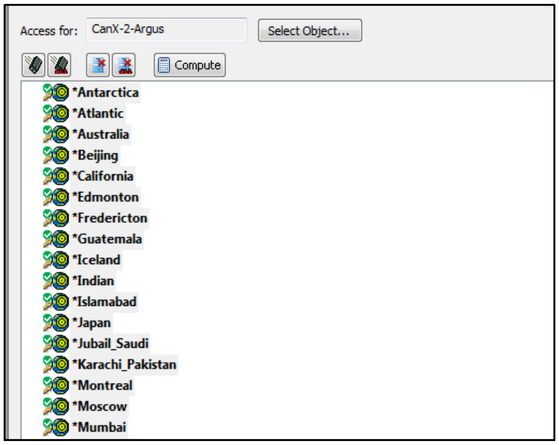

Access for: CanX-2-Argus

*Antarctica
*Atlantic
*Australia
*Beijing
*California
*Edmonton
*Fredericton
*Guatemala
*Iceland
*Indian
*Islamabad
*Japan
*Jubail_Saudi
*Karachi_Pakistan
*Montreal
*Moscow
*Mumbai

Figure 19: Sample of Argus targets in STK.

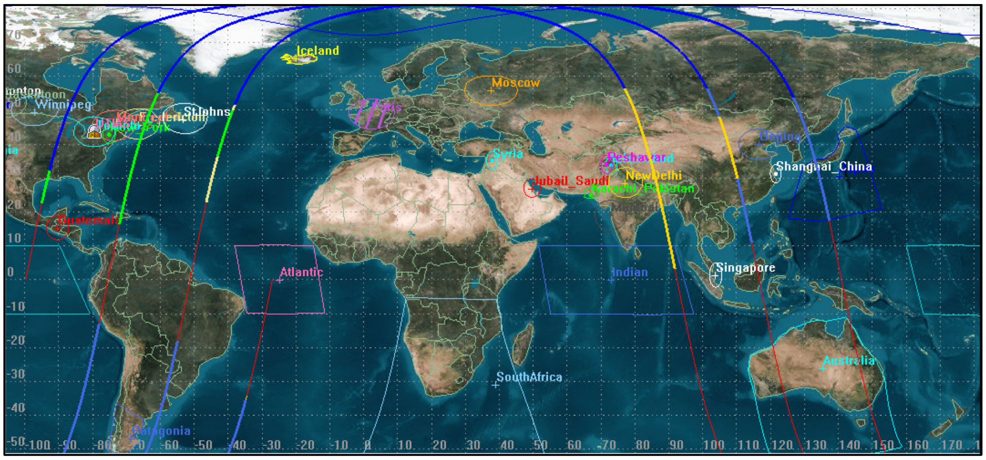

Figure 20: Some of Argus targets around the globe and CanX-2 passes over them.

Table 8: List of the selected targets for week 100 of January 19th, 2015.

Week	Start Time (UTCG)	Stop Time (UTCG)
100	2015/Jan/19 04:00:00.00	2015/Jan/23 04:00:00.00

Pass	Start Time (UTCG)	Stop Time (UTCG)	Duration (sec)
5	2015/Jan/19 10:41:35.35	2015/Jan/19 10:44:56.56	200.537
5	2015/Jan/19 10:48:06.06	2015/Jan/19 10:48:16.16	9.36
5	2015/Jan/19 10:54:13.13	2015/Jan/19 11:01:32.32	438.79
6	2015/Jan/19 12:16:41.41	2015/Jan/19 12:20:50.50	248.448
6	2015/Jan/19 12:22:54.54	2015/Jan/19 12:26:34.34	220.573
6	2015/Jan/19 12:30:27.27	2015/Jan/19 12:38:29.29	482.564
7	2015/Jan/19 13:54:06.06	2015/Jan/19 13:56:57.57	171.334
7	2015/Jan/19 13:58:37.37	2015/Jan/19 14:03:38.38	300.831
8	2015/Jan/19 15:34:30.30	2015/Jan/19 15:40:33.33	362.207
8	2015/Jan/19 15:30:56.56	2015/Jan/19 15:32:32.32	96.237
14	2015/Jan/20 01:10:14.14	2015/Jan/20 01:18:56.56	521.904
14	2015/Jan/20 01:28:25.25	2015/Jan/20 01:29:42.42	76.648
14	2015/Jan/20 01:10:14.14	2015/Jan/20 01:18:56.56	521.904
16	2015/Jan/20 03:57:12.12	2015/Jan/20 03:58:50.50	98.466
16	2015/Jan/20 03:57:12.12	2015/Jan/20 03:58:50.50	98.466

The operations team at UTIAS provides the Argus team with the data sets weekly during the observation campaign. The data sets consist of three files: a binary file that details Argus settings (exposure time, sensitivity, temperature) that were applied during the observation, the data file that has an extension *.CX2MEM containing the raw data collected over the selected target, and the attitude file that provides the satellite orientation information. Figure 21 illustrates the different types of the data files provided by the operations unit at UTIAS. Argus provides the raw data file, which consists of a series of data packets, to an onboard computer in 532 byte unsigned 8-bit words. Argus data packets are transmitted continuously at a cycle period determined as (256 milliseconds + Integration time) * (Number of Scans + 1). Table 9 describes Argus' packet format.

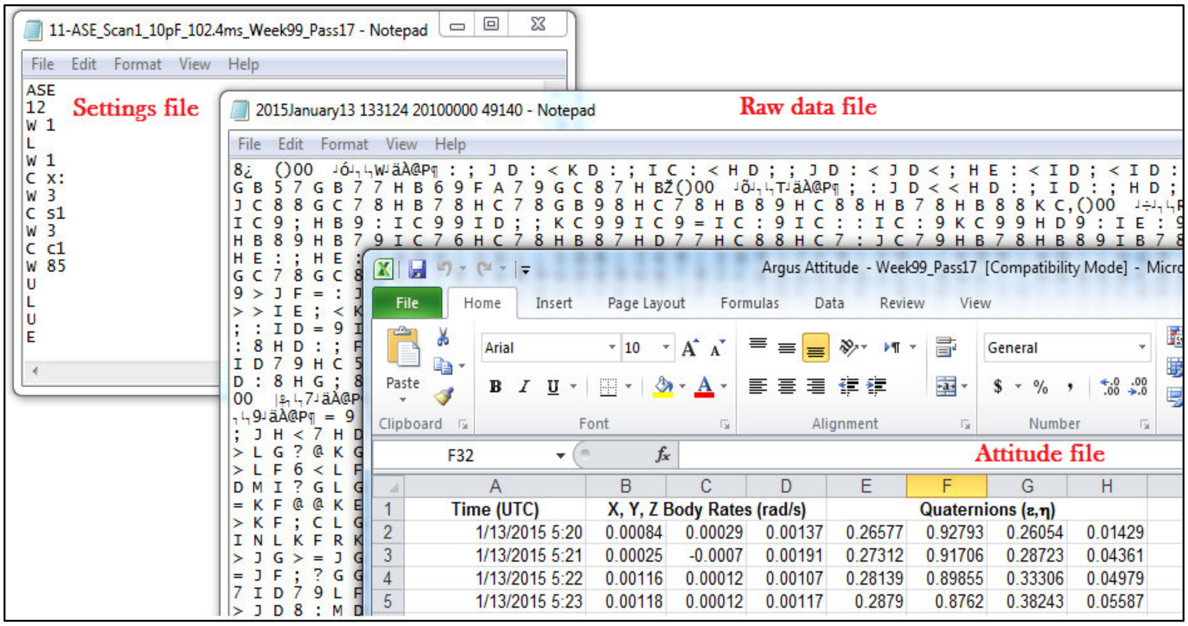

```
ASE
12
W 1
L
W 1
C x:
W 3
C s1
W 3
C c1
W 85
U
L
U
E
```

	A	B	C	D	E	F	G	H
1	Time (UTC)	X, Y, Z Body Rates (rad/s)			Quaternions (ε,η)			
2	1/13/2015 5:20	0.00084	0.00029	0.00137	0.26577	0.92793	0.26054	0.01429
3	1/13/2015 5:21	0.00025	-0.0007	0.00191	0.27312	0.91706	0.28723	0.04361
4	1/13/2015 5:22	0.00116	0.00012	0.00107	0.28139	0.89855	0.33306	0.04979
5	1/13/2015 5:23	0.00118	0.00012	0.00117	0.2879	0.8762	0.38243	0.05587

Figure 21: Data files provided by UTIAS for each pass in every observational campaign.

Table 9: Argus 1000 spectrometer Data Packet Format for CanX-2 flight model.

Word Number	Description
1-2	Synchronization Characters '(' and ')' provided to indicate packet start.
3-4	Device ID identifies Argus Instrument serial number [3] [4].
5-6	Command acknowledgement and errors provided in two-character format: [5] [6]. (Refer to section 12.1 in Argus manual, 2010).
7-8	Last command received provided in two-character format [7] [8] (Refer to section 12.1 in Argus manual, 2010).
9-12	Time since power on in Seconds computed as: [9]x(60x60x24) + [10]x(60x60) + [11]x(60) + [12].
13	Integration Time for Exposure in Seconds computed as: 2^[13] x 0.00005.
14	Number of scans to co-added before data transmission.
15	8-bit binary word comprising: [15 Bit 1] Dynamic Range Setting 0 = High Sensitivity, 1 = High Dynamic Range. [15 Bit 2] Cooler Temperature Setting 0 = High Temp, 1 = Low Temp. [15 Bit 3] Auto-exposure time setting 0 = Mode OFF, 1 = Mode ON.
16-17	Detector Temperature (DT) computed in degrees Celsius as: V0=3.25*([16]*256+[17])./1023;Rt=26.7e3*(3.22-V0)./(V0+1.78); DT=1/(1.289e-3 + 2.3561e-4 * ln(Rt) + 9.4272e-8 * (ln(Rt)^3));
18-19	Lifetime power ups computed as: [18]*256 + [19].
20-21	Adaptive exposure mode: pixel range for adaptive exposure defined as lower pixel number [21] to upper pixel number [20] to include.
22-23	Adaptive exposure mode: upper [22] and lower [23] thresholds to trigger changes in integration time expressed in percent of full dynamic range.
23-535	535 spectral data encoded as 512-bytes in repeating unsigned MSB and LSB 8-bit words [MSB]*256 + [LSB].
536	Parity word computed bitwise as: U (I=1...534) XOR(byte_i, byte_i+1)

2.4.5 Potential Instrument Improvements

CanX-2 satellite is considered to be the first generation of the CanX satellite series developed by UTIAS after the loss of CanX-1 in 2003. As previously mentioned, Argus 1000 spectrometer onboard of CanX-2 has been collecting data since 2008. Analysis of Argus 1000 data suggests that some improvements can be done to the instrument to enhance the quality of the data. One of the potential improvements is to employ glint mode which allows the instrument to point at the glint spot, where the sunlight is specularly reflected from the Earth's surface. This observation mode will improve the instrument SNR over dark surfaces like oceans. Moreover, for validation purposes, VIS or NIR camera can be installed alongside Argus 1000 spectrometer to image the scenes that the spectrometer is looking at.

3.0 Measurements Strategy

The Argus 1000 spectrometer is a passive remote sensing instrument that exploits the reflected sunlight from the atmosphere and Earth’s surface to monitor the atmospheric gases in the spectral interval 1000 to 1700 nm. As solar radiation propagates through the Earth’s atmosphere, it is affected by physical processes such as absorption, emission, and scattering that may be modelled by application of radiative transfer theory. The radiative transfer equations and the model used in this thesis are explored in the following section.

3.1 The Radiative Transfer Equation

The spectral features of the molecular absorption of the reflected radiation by specific gas species can be used to study the composition of the Earth’s atmosphere. In the absence of the scattering effects, the amount of absorption depends on the density of the gas and the length of the path. The interaction between solar radiation and atmospheric matter such as gases plays a key role for life conditions on Earth, thus investigating the radiative transfer process as well as the radiative properties of the solar radiation is of crucial significance. The Beer–Lambert law is one of the fundamental principles in measuring the radiative transfer in the atmosphere. It is the linear relationship between the absorbance and the concentration of an absorber. For one species, Beer–Lambert’s law states:

$$dI_\lambda = -I_\lambda \, K_\lambda \, \rho_l \, dl \qquad \textbf{(1)}$$

where I is the radiance ($\mathrm{W}m^{-2}sr^{-1}$), ρ_l is the number density of the absorbing gas (molecules m^{-3}), K_λ is the extinction cross section (m^2 molecules^{-1}) which is the sum of the absorption and scattering cross sections. The terms dl and dI_λ are the length of the path (m) and the attenuation (decrease) in the incident radiance, respectively. The negative sign represents the reduction in the incident radiance by the absorption and scattering that has been experienced in the medium. Figure 22 illustrates the Beer–Lambert law. The radiation's intensity may be enhanced by emission from the medium that is being traversed plus multiple scattering from all the directions. The increase in the radiation intensity due to emission and multiple scattering [Liou, 2002] is given by:

$$dI_\lambda = j_\lambda \, \rho_l \, dl \qquad \textbf{(2)}$$

Where j_λ is the source function coefficient, hence the importance of accounting for the source function, which is defined as ratio of the source function coefficient to the extinction coefficient $J_\lambda = {}^{j_\lambda}/_{K_\lambda}$ ($\mathrm{W}m^{-2}sr^{-1}$). By combining equations (1) and (2), we obtain:

$$dI_\lambda = -\, I_\lambda \, \rho_l \, K_\lambda \, dl + j_\lambda \, \rho_l \, dl \qquad \textbf{(3)}$$

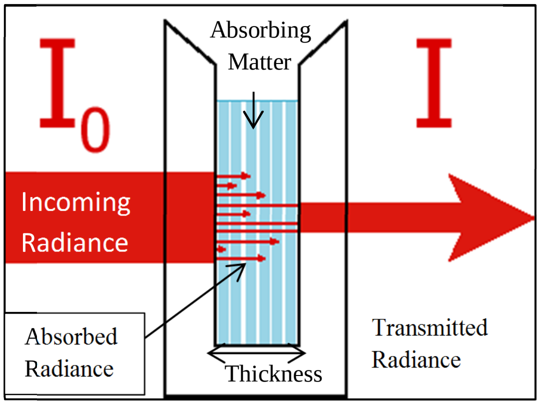

Figure 22: Illustration of energy transportation (Beer–Lambert Law).

By rearranging equation (3), it will yield:

$$\frac{dI_\lambda}{\rho_l\,K_\lambda\,dl} = -I_\lambda + J_\lambda \qquad \textbf{(4)}$$

Equation (4) is the general radiative transfer equation without any coordinate system imposed, which is fundamental to the discussion of any radiative transfer process [Liou, 2002]. It elucidates how the energy is lost by absorption, gained by atmospheric emission, and redistributed by scattering when a beam of radiation travels through the Earth's atmosphere.

3.2 The GENSPECT Radiative Transfer Model with Selectable Interpolation Error Tolerance

GENSPECT is a line-by-line radiative transfer algorithm for absorption, emission, and transmission for a wide range of atmospheric gases. Given information including gas types and amounts, pressure, path length, temperature, and frequency range for an atmosphere, the GENSPECT model computes the spectral characteristics of the gas. GENSPECT employs a new computation algorithm that maintains a specified accuracy for the calculation as a whole by pre-computing where a line function may be interpolated without a reduction in accuracy. The approach employs a binary division of the spectral range, and calculations are performed on a cascaded series of wavelength grids, each with approximately twice the spectral resolution of the previous one. The GENSPECT error tolerances are 0.01%, 0.1%, and 1% which may be selected according to the application [Quine & Drummond, 2002].

GENSPECT has been developed under MATLAB as a toolbox of components. The toolbox includes a library of functions and a library of scripts to illustrate how to carry out example calculations to model optical paths through planetary atmospheres or laboratory instrumentation [Quine & Drummond, 2002]. The GENSPECT algorithm was used in this analysis to model the radiance that follows a single path under the effect of different parameters and the results will be explored in the following chapter.

3.3 The Sensitivity Analysis Methodology

Radiance measurements from space at any CO_2 absorption band can be used to determine the total column CO_2 amount. For Argus therefore, we focus on the instrument response at 1580 nm and 1600 nm bands to boundary layer atmospheric CO_2 changes in relation to the response to other variables. The vibrational–rotational CO_2 solar infrared band at 1580 nm will, partially, allow solar radiation to pass through the whole atmosphere and be reflected back to space by Earth's surface. The upwelling radiance at the top of the atmosphere is therefore sensitive to the total column CO_2 abundance [Mao & Kawa, 2004].

Incoming solar radiation is attenuated as it penetrates the atmosphere, reflects from the surface, and travels back to space. In the real atmosphere, the attenuation in the 1580 nm band includes molecular scattering, absorption by CO_2 and other gases such as H_2O, extinction (scattering plus absorption), and partial reflection at the Earth's surface.

As previously mentioned, we focus on the back-to-space radiance response to a CO_2 change under various geophysical conditions. In this analysis, the sensitivity of back-to-space radiance to the change of CO_2 concentration was performed by adjusting the whole atmospheric column as well as the concentration in the atmospheric boundary layer where CO_2 varies the most. GENSPECT code was used to show the advantage of selecting the CO_2 band at 1.58 µm and its sensitivity to the back-to-space radiance. The radiance change was plotted when the CO_2 mixing ratio is increased by 0.28% (~1 ppmv) in the whole column (0–50 km) and 1% (3.6 ppmv) in the atmospheric boundary layer (0–2 km in the atmosphere).

Solar insolation depends strongly on the solar zenith angle θ and also on the ratio $(^{d}/_{d_m})$ of the actual distance, which changes as Earth orbits the sun in an elliptical orbit, to the mean distance of the Earth from the Sun [Fu Q., 2002]. Incident light has more intensity and less attenuation when it makes a 90° angle with Earth's surface (at SZA of 0°) like in case B in Figure 23. On the other hand, light has less intensity and more attenuation in the atmosphere when it falls in a shallow angle like in case A in Figure 23. In this study, back-to-space radiance was investigated under two different solar zenith angles (SZAs), 30° and 80°, in order to examine the SZA variation effect.

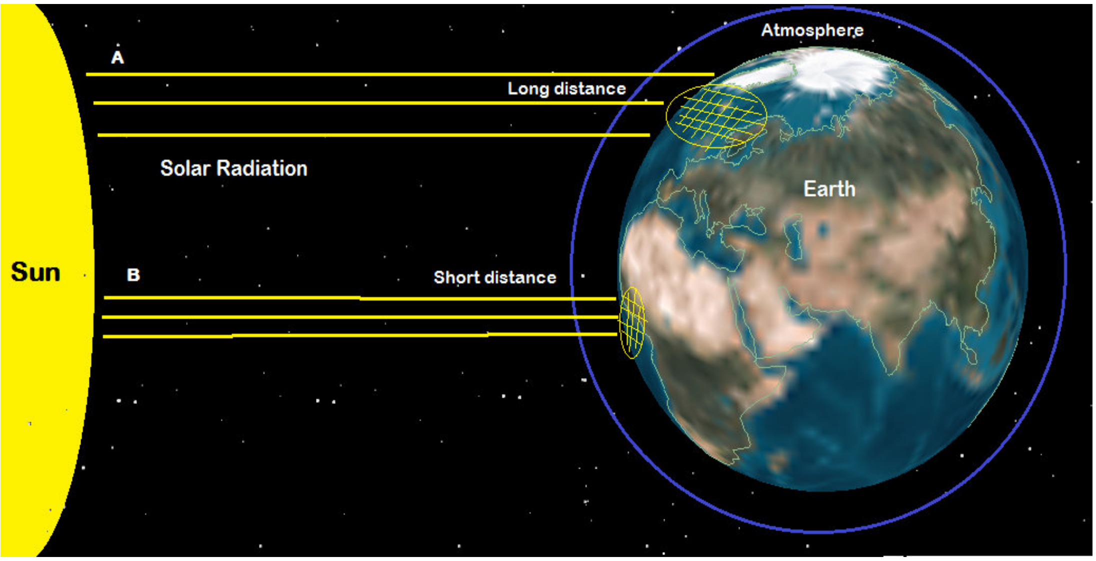

Figure 23: Solar radiation when strikes the Earth's surface at a large zenith angle (A) and when it makes a small zenith angle (B).

The solar radiation path was examined in the model assuming two scenarios that the solar radiance might experience. In the first scenario, the solar beam is assumed to reach the ground and reflect back to space. In the second scenario, the solar beam is reflected off a cloud layer, which is 4 km above the ground, back to space. The ratio between beams in both scenarios is calculated.

A geolocation algorithm is used [Benari, 2012] to locate Argus 1000 spectrometer flight data as well as the CanX-2 satellite observational path. In order to assess and validate the quality of Argus spectrometer data, pseudo-true color Advanced Very High Resolution Radiometer (AVHRR) cloud imagery [Space Science and Engineering Centre, 2009] is used. Google Earth software is used to view the data sets and granules in question.

4.0 Results and Discussion

4.1 Argus 1000 Spectrometer Spectral Range

The Argus 1000 spectrometer operates in the spectral range from 1 to 1.7 microns (Short Wavelength InfraRed-SWIR) where we observe some greenhouse gas absorption features. Figure 24 illustrates Argus synthetic spectra (radiance and smoothed radiance) and the GHG absorption positions. Figure 25 shows only the smoothed radiance, which provides a better visualization.

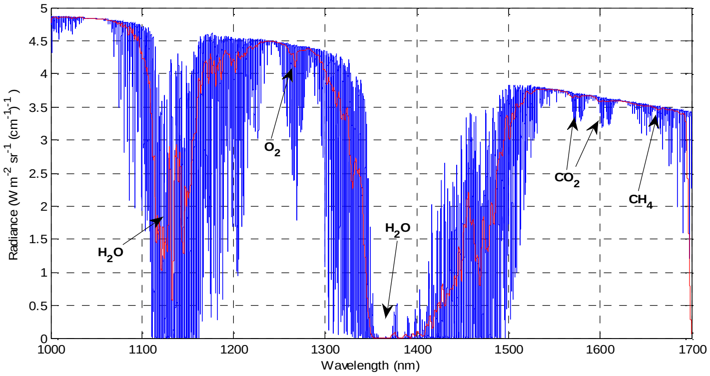

Figure 24: Argus Synthetic Spectra in GENSPECT and the positions of absorbing gases

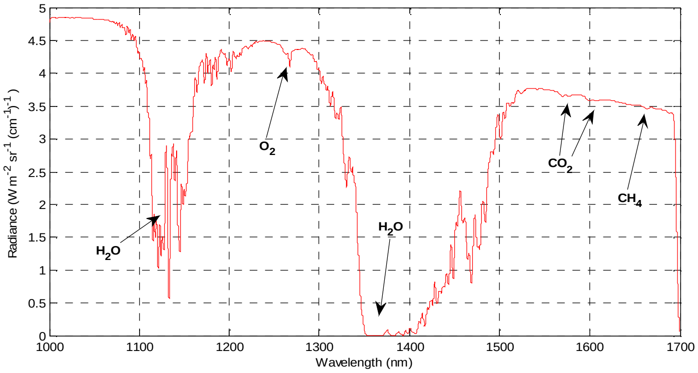

Figure 25: Argus synthetic smoothed radiance (W m^{-2} sr^{-1} $(cm^{-1})^{-1}$) in the model and the gas absorption band positions in the spectral range from1 to 1.7 microns.

This sensitivity analysis utilizes the CO_2 absorption of reflected sunlight near 1.58 microns. Figure 26 shows the CO_2 bands at 1.58 and 1.60 μm after zooming in on the SWIR range for a Nadir viewing geometry and 30° solar zenith angle. Space-based radiance measurments of the CO_2 band near 1.58 μm have less sensitivity to the atmospheric temperature and water vapor interference is minimal. Figure 27 illustrates the vibrational–rotational CO_2 radiance band at the SWIR range near 1.58 μm. The solar infrared band of CO_2 at 1.58 μm allows the solar radiation to partially penetrate the whole atmosphere and be reflected back to space by the Earth's surface [Mao & Kawa, 2004].

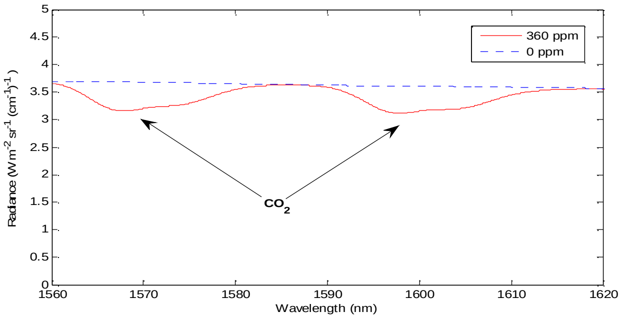

Figure 26: Carbon dioxide bands at 1.58 and 1.60 μm. Notice the CO_2 concentration 0 ppm (dashed blue line) and 360 ppm (red line).

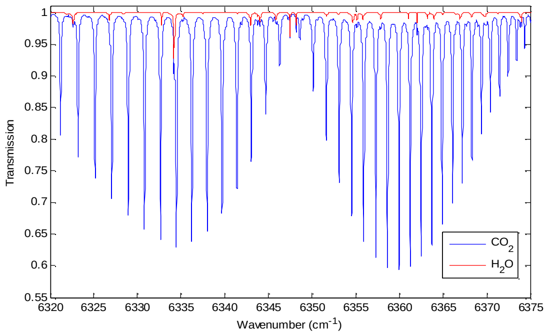

Figure 27: One way (space-to-ground) radiation transmittance of CO_2 (blue line) and H_2O (red line) in the 1568-1582 nm band at Nadir viewing geometry. 1976 U.S Standard Atmosphere was used in the calculation. Notice the minimal interference of H_2O in this band

The carbon dioxide band in Figure 27 is characterized by two groups of absorption lines known as **P** (corresponding to the rotational transition where $\Delta J = -1$) and **R** (corresponding to rotational transition where $\Delta J = +1$) branches. **P** and **R** are separated by a gap close to the centre of the band ~6347.85 cm^{-1}. The absorption lines in each branch are nearly equally spaced. It is clearly seen from Figure 28 that the line spacing in the higher-frequency branch is slightly narrower than that in the lower-frequency branch. As mentioned above, the band has the least water-vapour (H_2O) interference (red line in Figure 27), thus it provides a sufficient radiance signal for atmospheric total column CO_2 detection compared with other CO_2 bands in the solar infrared [Mao & Kawa, 2004]. Moreover, the sensitivity to temperature in this band is minimized, in contrast to other candidate bands at 15 and 4.3 μm where the sensitivity of space-based radiance to emission temperature is larger than the sensitivity to the CO_2 mixing ratio change [McMillin & Fleming, 1976].

4.2 Measurement Sensitivity to CO_2 Concentration Change

The carbon dioxide concentration in the air has increased by approximately one third since pre-industrial times in 1750 and increased by approximately 0.43% (1.5 ppmv/yr) in the 1990s [IPCC, 2001]. Modern CO_2 measurement strategies retrieve the atmospheric CO_2 column by fitting the logarithm of the measured ratio of nadir radiance and solar radiative flux (irradiance). The sensitivity of the back-to-space radiance with respect to CO_2 concentration is investigated in this section. In this sensitivity study, the solar zenith angle is selected to be a moderate value of 30° and the satellite viewing geometry is chosen to be Nadir, which is the current viewing mode of the Argus 1000 spectrometer in space. The baseline atmospheric CO_2 concentration value is set to 360 ppmv. Table 10 lists the baseline input parameters of the radiance simulations in the model.

Table 10: Parameters used in the analysis

Parameter	Value
1976 U.S Standard Atmosphere	0–50 km and 0–2 km
CO_2 Mixing ratio	360 ppm
Surface	Lambertian
Reflectance (Albedo)	0.3
Solar Angle	30° and 80°
Satellite Viewing Angle	Nadir
Calculation Resolution	8×10^{-3} cm^{-1}
Atom Isotope	All isotopes
Database Type	Hitran

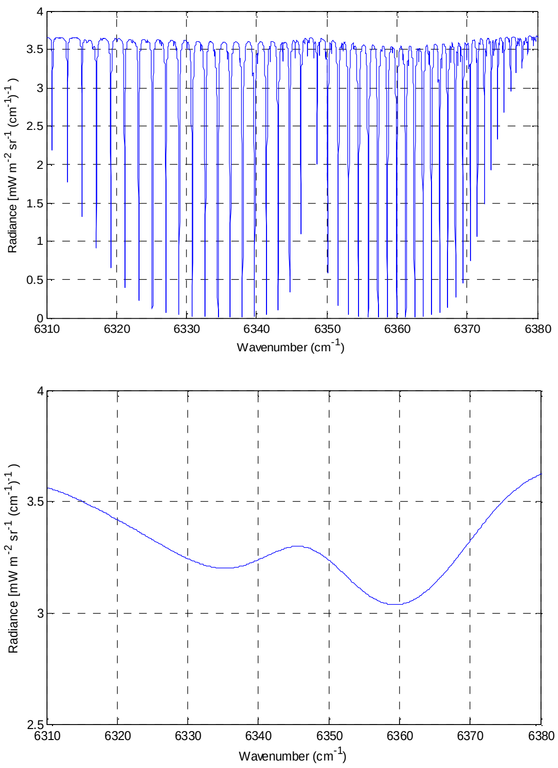

Figure 28: Top panel, the Nadir viewing back-to-space radiance (mW m^{-2} sr^{-1} (cm^{-1})$^{-1}$) at solar zenith angle 30° in the whole atmospheric column (0–50 km); bottom panel, the smoothed back-to-space radiance at SZA 30° in the whole column.

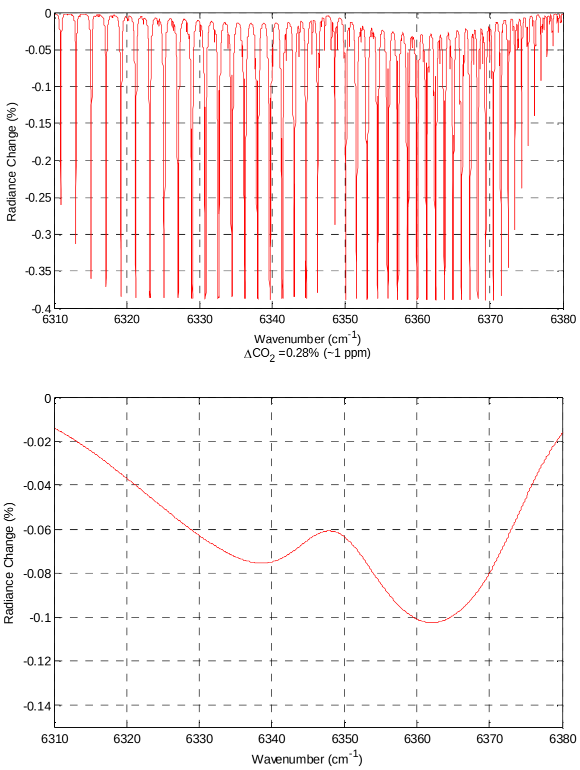

Figure 29: Top panel, the radiance sensitivity to ~0.28% (1-ppmv) CO_2 concentration increase in the whole column; bottom panel, the smoothed radiance sensitivity to 1 ppm mixing ratio change in the whole column.

Figure 28 (Top panel) shows synthetic back-to-space radiance over the spectral range from 6310 cm^{-1} to 6380 cm^{-1} (1567 to 1584 nm) when the CO_2 mixing ratio is 360 ppmv in the whole column while the bottom panel in the same figure displays the smoothed spectrum for the same back-to-space radiance in the total column. GENSPECT smoothing functions were used to smooth the spectra to Argus 1000 resolution (6nm).

The radiance change (%) was performed in GENSPECT according to the following equation:

$$\frac{I_{GEN_{In}}-I_{GEN_{St}}}{I_{GEN_{St}}} \qquad \textbf{(5)}$$

where $I_{GEN_{In}}$ is the radiance after increasing the $\mathrm{CO_2}$ mixing ratio in GENSPECT and $I_{GEN_{St}}$is the radiance at GENSPECT's $\mathrm{CO_2}$ standard concentration.

As shown in Figure 29 (Top panel), increasing the atmospheric $\mathrm{CO_2}$ concentration by approximately 0.28% (1 ppmv) uniformly in the whole atmospheric column yielded a negative change in the synthetic back-to-space solar radiance, which decreased up to 0.38% (at 0.008 $\mathrm{cm^{-1}}$ spectral resolution) because radiance transmittance decreases with increased amount of $\mathrm{CO_2}$ in the atmosphere. The Back-to-space radiance decreases up to 0.10% at Argus 1000 spectral resolution (6 nm) as shown in the smoothed spectrum at the bottom panel in Figure 29. Certainly, spectral resolution plays a key role in the $\mathrm{CO_2}$ retrieval process.

The back-to-space radiance behaviour for $\mathrm{CO_2}$ change in the atmospheric boundary layer (0-2 km) differs from its behaviour for the same $\mathrm{CO_2}$ change in the whole column (0-50 km). Figure 30 (Top panel) shows the back-to-space radiance (mW $\mathrm{m^{-2}}$ $\mathrm{sr^{-1}}$ $\mathrm{(cm^{-1})^{-1}}$) at solar zenith angle (SZA) 30° when the $\mathrm{CO_2}$ mixing ratio increases by 1% (3.6 ppm) in the atmospheric boundary layer. The bottom panel in Figure 30 displays the smoothed back-to-space radiance to show the exact spectrum that the Argus 1000 would observe. Increasing the $\mathrm{CO_2}$ concentration in the atmospheric boundary layer (0-2 km) by 1% (3.6 ppmv), which is equivalent to the seasonal variability of $\mathrm{CO_2}$, will reduce the back-to-space radiance by up to 0.25% at 0.005 $\mathrm{cm^{-1}}$ spectral resolution (top panel in Figure 31) and approximately 0.05% when the spectrum is smoothed to Argus spectral resolution (bottom panel in Figure 31). Based on the median radiance change which is roughly 0.15% in the top panel of Figure 31, Mao and Kawa [2004] suggested that the signal-to-noise ratio must be at least 700:1 for a spectrometer to be able to detect 1% $\mathrm{CO_2}$ perturbation in the atmospheric boundary layer (0-2 km). However, when smoothed to Argus resolution (6 nm) as shown in the bottom panel of Figure 31, the radiance change at R branch center is approximately 0.05%. This implies that the Argus 1000 SNR must be at least 2000:1 to detect a 1% $\mathrm{CO_2}$ change in the atmospheric boundary layer (0-2 km). The instrument SNR is discussed in details in the next section.

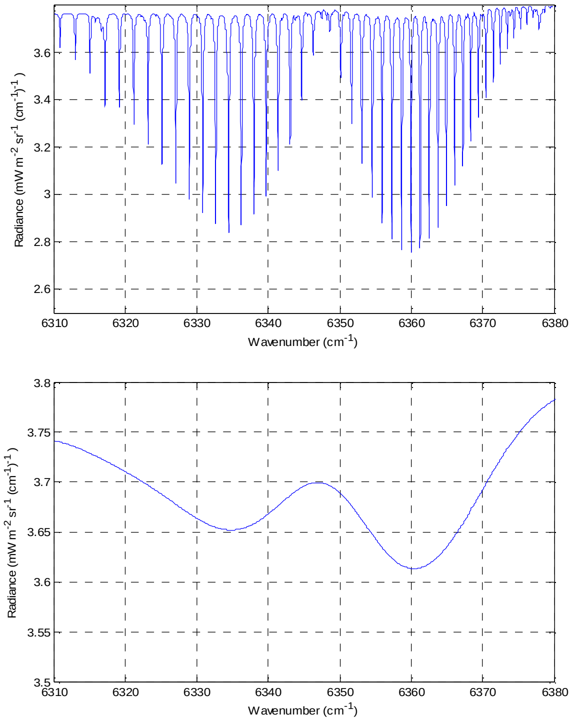

Figure 30: Top panel, the Nadir viewing back-to-space radiance (mW $\mathrm{m^{-2}}$ $\mathrm{sr^{-1}}$ $\mathrm{(cm^{-1})^{-1}}$) at solar zenith angle 30° in the atmospheric boundary layer ABL (0–2 km); bottom panel, the smoothed back-to-space radiance at SZA 30° in the ABL.

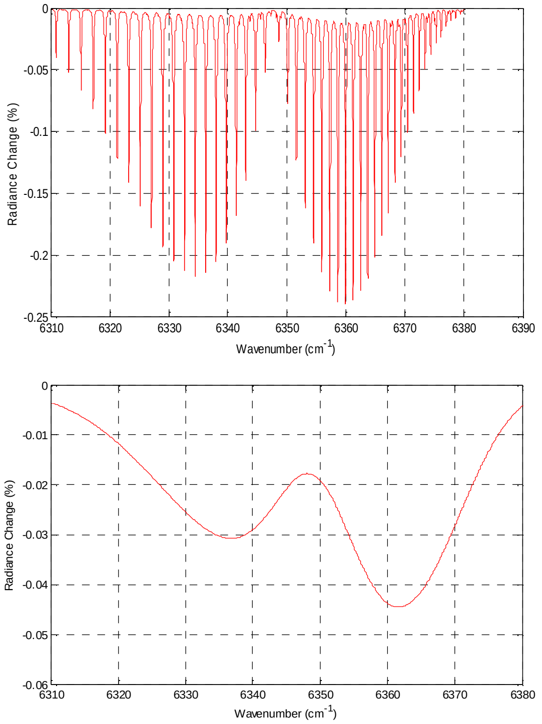

Figure 31: Top panel, the radiance sensitivity to 1% (3.6 ppmv) $\mathrm{CO_2}$ concentration increase in the atmospheric boundary layer ABL (0–2 km); bottom panel, the smoothed radiance sensitivity to a 3.6 ppm mixing ratio change in the ABL.

Wange et al [2014] discussed the retrieval accuracy and the required SNR for the TanSat (CarbonSat) instrument to detect a very small change (1%) $\mathrm{CO_2}$ near the Earth’s surface. Their results show that the required instrument SNR should be at least 900:1 to detect 1% $\mathrm{CO_2}$ change in the atmospheric boundary layer (0-2 km).

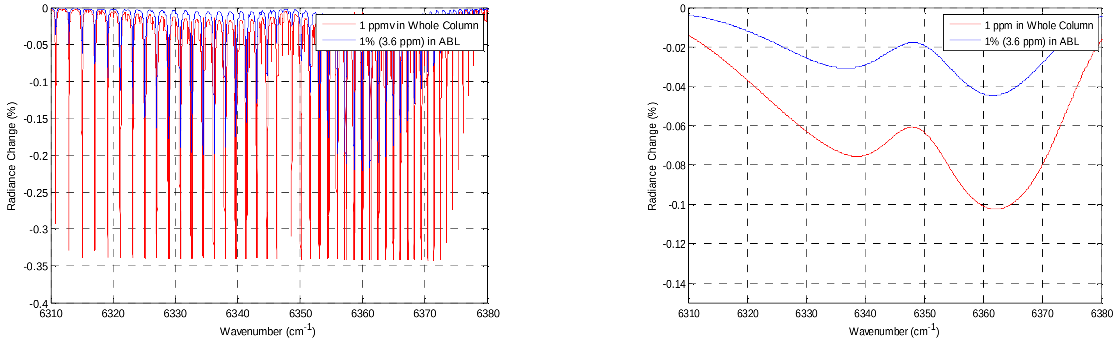

Figure 32: Right panel; comparison between radiance sensitivities to 0.28% (1-ppmv) CO_2 concentration increase (red line) in the whole column (0-50 km) and to a 1% (3.6 ppm) CO_2 mixing ratio increase (blue line) in the boundary layer (0-2 km). Left panel; smoothed spectra of the comparison in the right panel. Both radiance changes were calculated for SZA 30°.

Figure 32 compares the radiance changes when CO_2 is perturbed by 1% (3.6 ppmv) and 0.28% (1 ppmv) in the atmospheric boundary layer (0-2 km) and the whole column (0-50 km), respectively. The right panel of Figure 32 suggests that the radiance change for a 1% (3.6 ppm) CO_2 perturbation in the atmospheric boundary layer is approximately equivalent to 70% of the radiance change when CO_2 changes by 0.28% (1 ppmv) in the whole column. In the case of the Argus 1000 spectrometer, the radiance change for CO_2 perturbation in the boundary layer (0-2 km) is approximately 50% of the radiance change for CO_2 perturbation in the whole column (0-50 km) as shown in left panel in Figure 32. The radiance sensitivity to CO_2 changes in the near transparent region between the P and R branches is relatively week in the atmospheric boundary layer (0-2 km) compared to the case in the whole column (0-50 km).

Solar zenith angle is another significant parameter that must be taken into account when making measurements of reflected solar radiance at high latitudes. Large solar zenith angle imply low intensity (low SNR) and longer path length. Figures 33 and 34 show the back-to-space radiances at SZAs of 30° and 80°, respectively. It is clearly seen that the back-to-space radiance at SZA of 80° is approximately 1/5 of that at SZA of 30° and the atmospheric path length to the ground is five times longer. The reflectivity surface type is assumed to be Lambertian with an albedo value of 0.3. Different types of surfaces and multiple scattering will affect the back-to-space radiance at large SZA.

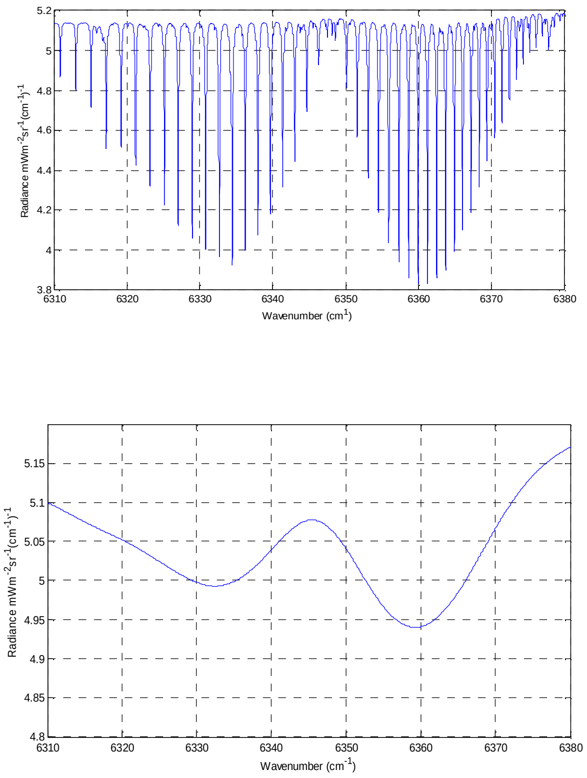

Figure 33: Top panel, the back-to-space radiance (mW m^{-2} sr^{-1} $(cm^{-1})^{-1}$) at SZA of 30°. Bottom panel, the smoothed top-of-the atmosphere radiance at the same SZA.

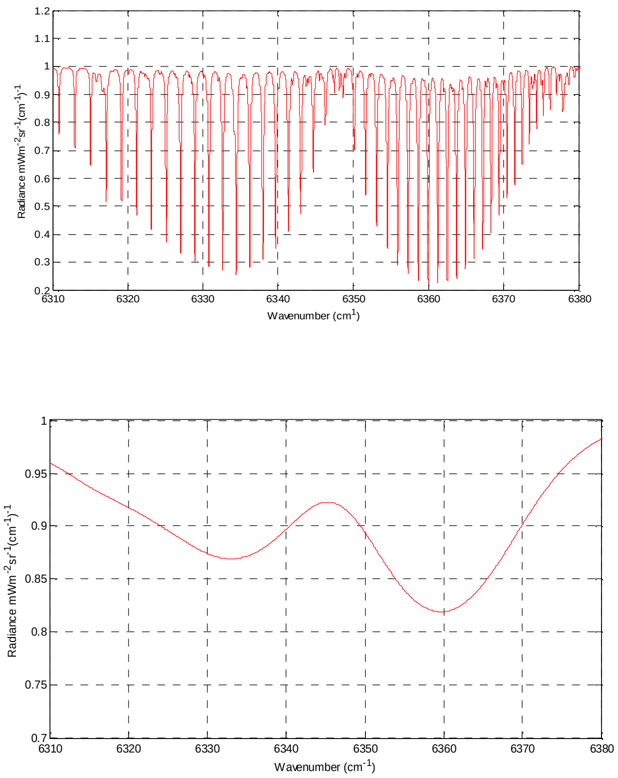

Figure 34: Top panel, the back-to-space radiance (mW m^{-2} sr^{-1} $(cm^{-1})^{-1}$) at SZA of 80°. Bottom panel, the smoothed top-of-the atmosphere radiance at the same SZA.

Table 11 illustrates the absorption minima (mW m^{-2} sr^{-1} $(cm^{-1})^{-1}$) at SZA 30° and 80°, respectively. Higher values mean less absorption, as in case of SZA 30°. However, instrumental dynamic range and SNR issues as well as the potential problems of low surface reflectance for snow and ice in this band must be overcome in order to be able to have a good sensitivity to CO_2 at high latitudes or near dawn and dusk [Mao & Kawa, 2004].

Table 11: Absorption minima corresponding to different SZAs.

Solar Zenith Angle (SZA) degrees	Absorption minimum $(\mathrm{mW\ m^{-2}\ sr^{-1}\ (cm^{-1})^{-1}})$
30°	**4.94***
80°	**0.82***

*Radiance values $(\mathrm{mW\ m^{-2}\ sr^{-1}\ (cm^{-1})^{-1}})$ in the bottom panels of Figures 33 and 34

4.2.1 Argus 1000 Signal-to-Noise Ratio

A laboratory experiment was setup in order to evaluate the current SNR of a flight spare Argus spectrometer. Figure 35 shows the preliminary setup for the laboratory experiment where Argus is able to read the signal reflected from the spectralon (white reflective screen) after collimating the light from the halogen bulb. The instrument was operated for 30 minutes and continuously collected data. Pixel number 242, which correlated to the $\mathrm{CO_2}$ amount, was chosen for analysis. The exposure time was set to 256mS with number of scans set to 2 (co-add) similar to Argus settings in space.

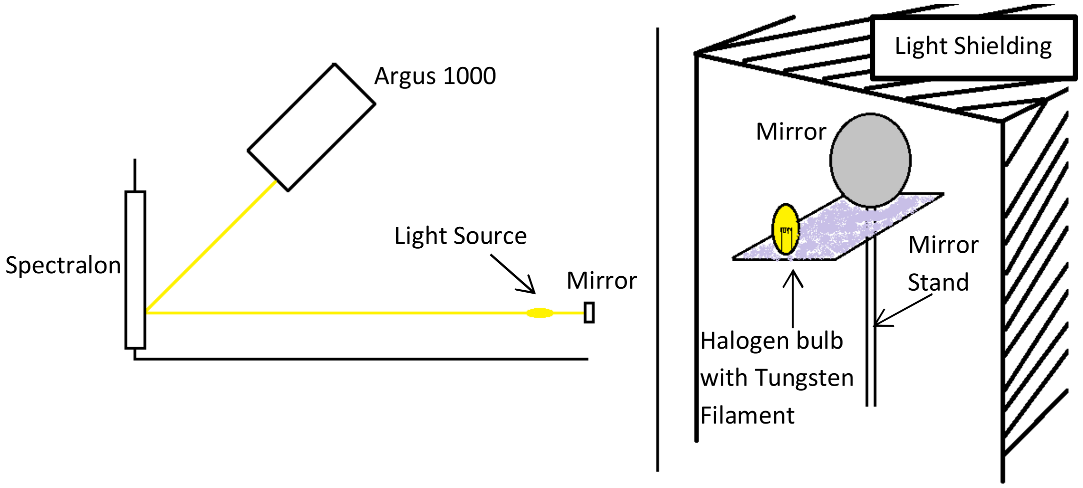

Figure 35: Laboratory experiment setup top view (left) and mirror and light source (right). [Image credit: Catherine Tsouvaltsidis & Naif Al Salem]

The signal's mean (μ) of pixel 242 was calculated as follows:

$$\mu = \frac{1}{N} \sum_{i=0}^{N-1} x_i \qquad \textbf{(6)}$$

Where the sum of the values, x_i, in the signal is divided by the number of samples *N*. The standard deviation (σ) of the signal is also calculated as follows:

$$\sigma^2 = \frac{1}{N-1} \sum_{i=0}^{N-1} (x_i - \mu)^2 \qquad \textbf{(7)}$$

The signal-to-noise ratio (SNR) of a signal is defined as mean (μ) of the signal divided by the standard deviation (σ) of the same signal as follows:

$$\text{SNR} = \frac{\boldsymbol{\mu}}{\boldsymbol{\sigma}} \qquad \textbf{(8)}$$

Figure 36 shows the instrument signal at pixel 242 where the mean (solid red line) and standard deviation (dashed red line) of the signal are outlined on the graph. The mean of the signal is 1514 and standard deviation (noise) is approximately 2.19 counts yielding an SNR value of approximately 691:1. If there are n pixels each with signal S, the SNR for one pixel, assuming the statistics are Poissonian, is calculated as following:

$$\text{SNR}_1 = \frac{S}{\sqrt{S}} = \sqrt{S} \qquad \textbf{(9)}$$

The total SNR for 5 pixels, which is the number of pixels related to the CO_2 amount, with signals approximately equal to S is calculated as following:

$$\text{SNR}_{\text{tot}} = \frac{5 \times S}{\sqrt{5 \times S}} = \sqrt{5 \times S} \qquad \textbf{(10)}$$

Therefore,

$$\text{SNR}_{\text{tot}} = \ = \sqrt{5} \times \text{SNR}_1 \qquad \textbf{(11)}$$

Yielding a total SNR of 1520:1 which is capable to detect approximately 1.31% of $\mathrm{CO_2}$ variation in the ABL. Figure 37 shows the instrument signal at pixels 240, 241, 246 and 247, respectively. Table 12 lists means, STDs, and SNRs of all pixels shown in Figure 37. In the SNR calculation, 1σ error was chosen to obtain a good quality data.

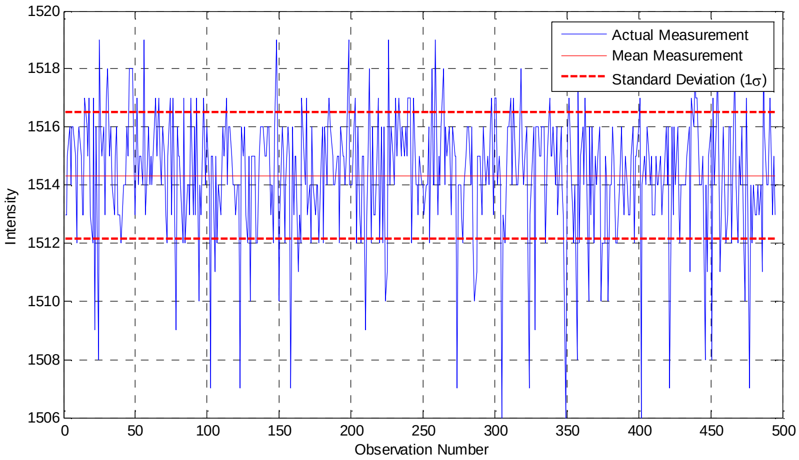

Figure 36: Instrument signal at pixel number 242.

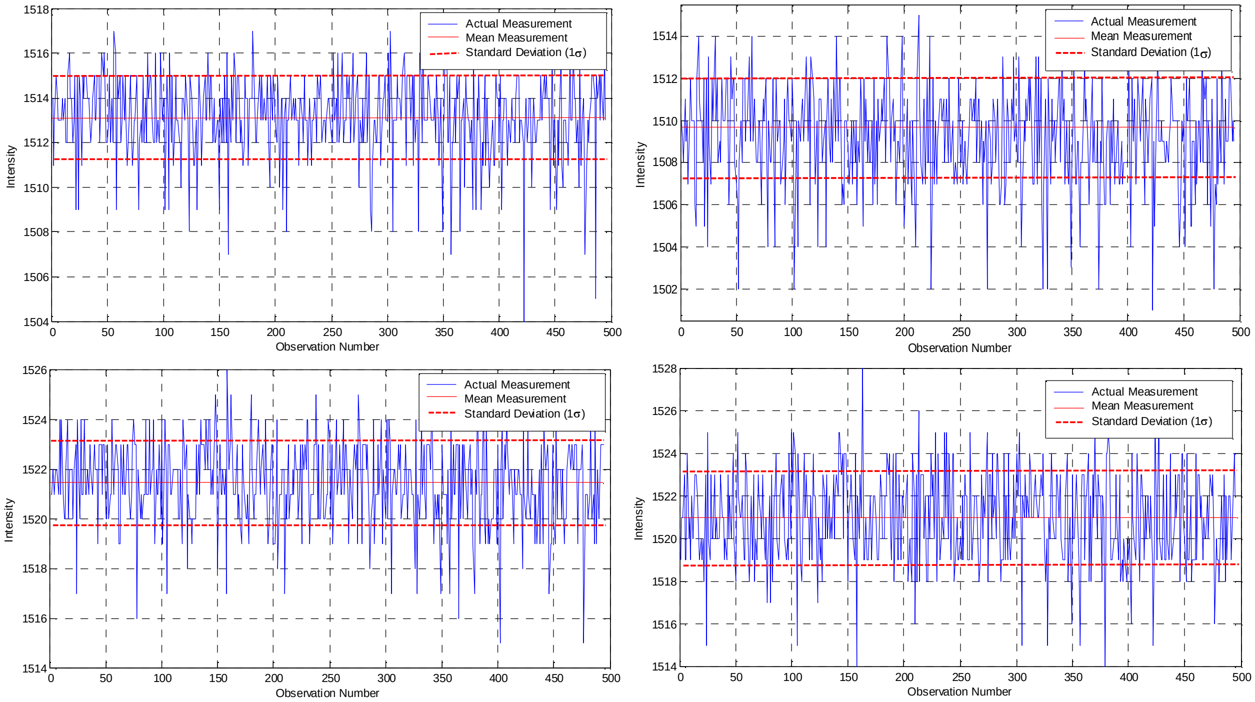

Figure 37: Instrument signal at pixel 240 (top left), 241 (bottom left), 246 (top right) and 247 (bottom right).

Table 12: Mean values, STDs and SNRs of all pixels shown in Figure 37

Pixel Number	**Mean**	**STD**	**SNR**
240	1513	1.86	813:1
241	1521	1.72	884:1
242	1514	2.19	691:1
246	1509	2.36	639:1
247	1521	2.17	700:1

Argus spectrometer has approximately five pixels correlated with CO_2 amount [Jagpal, 2011]. The SNR can be enhanced by either increasing the number of scans (temporal averaging) or averaging the number of pixels (spatial averaging); therefore, the SNR can be improved by a factor of approximately 2.2 which is the square root of the 5 pixels. The SNR can, also, be improved by the square root of the maximum co-add setting of 10, or a factor of 3, in the instrument; however, the spatial resolution will be degraded.

4.3 Solar Radiation Path Scenarios

Two scenarios that the solar radiation might follow are examined in the model. In the first scenario, the solar radiation reaches and reflects off the Earth's surface back to space. In the second scenario, the solar radiation reflects off a cloud layer that is approximately 4 km above the ground. Figure 38 illustrates the two scenarios that the solar radiation could experience in its journey from space through the atmosphere to the Earth's surface and back to space towards the sensor. The solar radiances $\mathrm{I}_{\mathrm{dir}}$ and $\mathrm{I}_{\mathrm{rfc}}$ are the direct beam reflected off the ground and the beam reflected off the cloud layer, respectively.

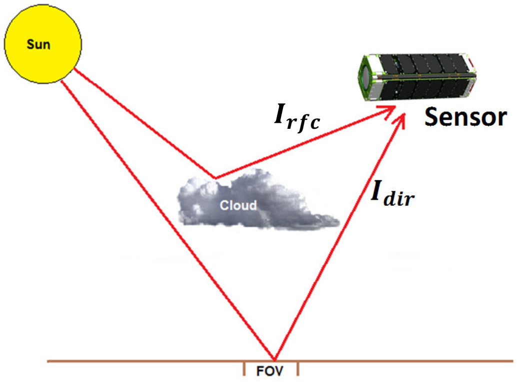

Figure 38: Illustration of possible scenarios as solar radiation passes through the atmosphere and back to space to reach the sensor. I_{dir} is the solar radiation beam directly reflected by the Earth's surface toward the sensor field of view (FOV). I_{crf} is the solar beam reflected off clouds.

The synthetic solar radiation beams that reflected off ground and cloud are shown in Figure 39. The solar beam that reached the ground and reflected back to space (left panel) yielded approximately 26.7 W m^{-2} sr^{-1} $(\mathrm{cm}^{-1})^{-1}$ while the solar beam that reflected off the cloud layer yielded about 120 W m^{-2} sr^{-1} $(\mathrm{cm}^{-1})^{-1}$. The ratio between the beams reflected off ground and cloud is approximately 4.5. Solar radiance that reaches the ground travels through long atmospheric path and experience more energy loss (attenuation) while the solar beam reflected off cloud travels through short atmospheric path and experience less energy reduction. Table 13 lists the model parameters used in the solar radiance path scenarios.

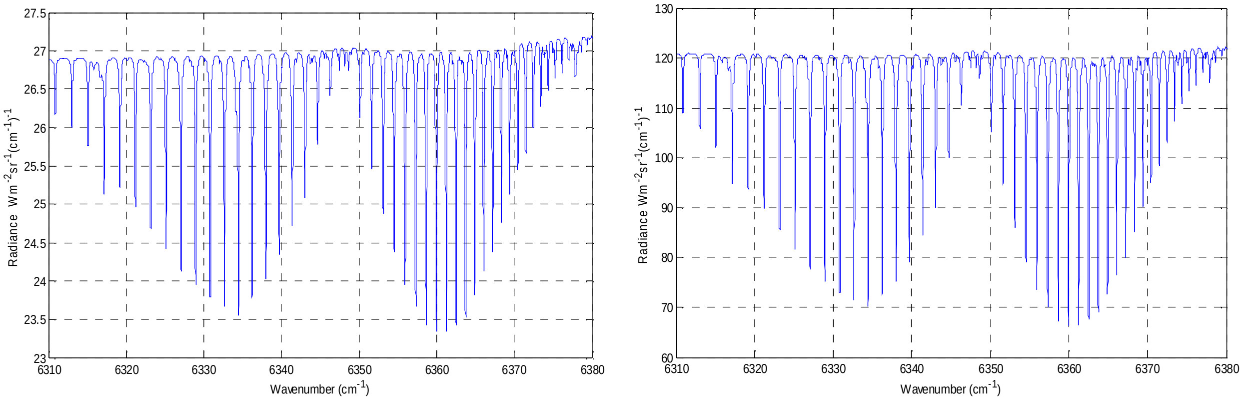

Figure 39: Synthatic solar beams reflected off ground (left panel) and off cloud (right panel) at SZA of 30°.

Table 13: Model parameters used in the path scenario calculation.

Parameter	Value
SZA	30°
Albedo	0.2 (land) and 0.9 (Cloud)
Cloud height	4 km
Surface	Lambertian

4.4 Effects of Clouds on Solar Radiation and CO_2 Absorption

In the atmosphere, reduction in the solar radiation near the 1.58-μm band includes some atmospheric processes such as molecular scattering, absorption by CO_2, and other atmospheric gases such as H_2O and CH_4, extinction by aerosols, and partial reflection at Earth's surface. The absorbed radiation is added directly to the heat budget, whereas the scattered radiation is partly returned to space and partly continues its path through the Earth–atmosphere system where it is subject to further scattering and absorption [Fu, Q., 2002].

Clouds cover about 65% of the Earth and are the most important regulator of solar radiation. By reflecting incoming solar radiation back to space, they cool the Earth–atmosphere system–the so-called cloud albedo effect which depends on cloud type and cloud form, as well as the solar zenith angle. Clouds also absorb solar radiation in the near infrared region [Fu, Q., 2002]. They appear to absorb up to 20% of the solar energy incident on them, with solar heating rates reaching over 2 $K\ h^{-1}$ near cloud tops [Slingo and Schrecker, 1982]. The previous numbers are not definitive, however, and our understanding of cloud absorption remains limited from both observational and theoretical perspectives [Davies, Ridgway, and Kim, 1984].

Cloud presence in the atmospheric boundary layer could lead to a variation of CO_2 absorption at 1575 nm. Clouds could reflect some fraction of the incident solar radiation, preventing it from reaching the Earth's surface and therefore leading to an underestimation of the CO_2 absorption under the cloud layer. Some fraction of the solar radiance could perform multiple reflections under the cloud layer, leading to an overestimation of the CO_2 absorption in the SWIR range.

The effect of clouds on both solar radiation and CO_2 absorption is analyzed using some flight data collected by the Argus 1000 spectrometer over cloudy and cloud-free scenes. Figure 40 shows some flight data collected for week 41 pass 34, week 9 pass 36 and week 77 pass 28, respectively. Argus 1000 collected these data over some cloudy and clear scenes as it shows in the first row of Figure 40. The second row in the same figure shows the normalized radiance of cloudy and clear spectra at the CO_2 band 1575 nm. The third row illustrates the actual cloud cover for the geolocated packet numbers. The cloud cover data is retrieved from MODIS

(MODerate Resolution Imaging Spectroradiometer) as well as the AVHRR (Advanced Very High Resolution Radiometer). Table 14 lists the packet number geolocation parameters.

The ratio between normalized cloudy and clear spectra in Figure 40 indicates that the CO_2 absorption in the absence of clouds is higher than when clouds are present by approximately 5.3%. The atmospheric column path is longer in clear sky than cloudy sky and therefore photons will experience less absorption in the later.

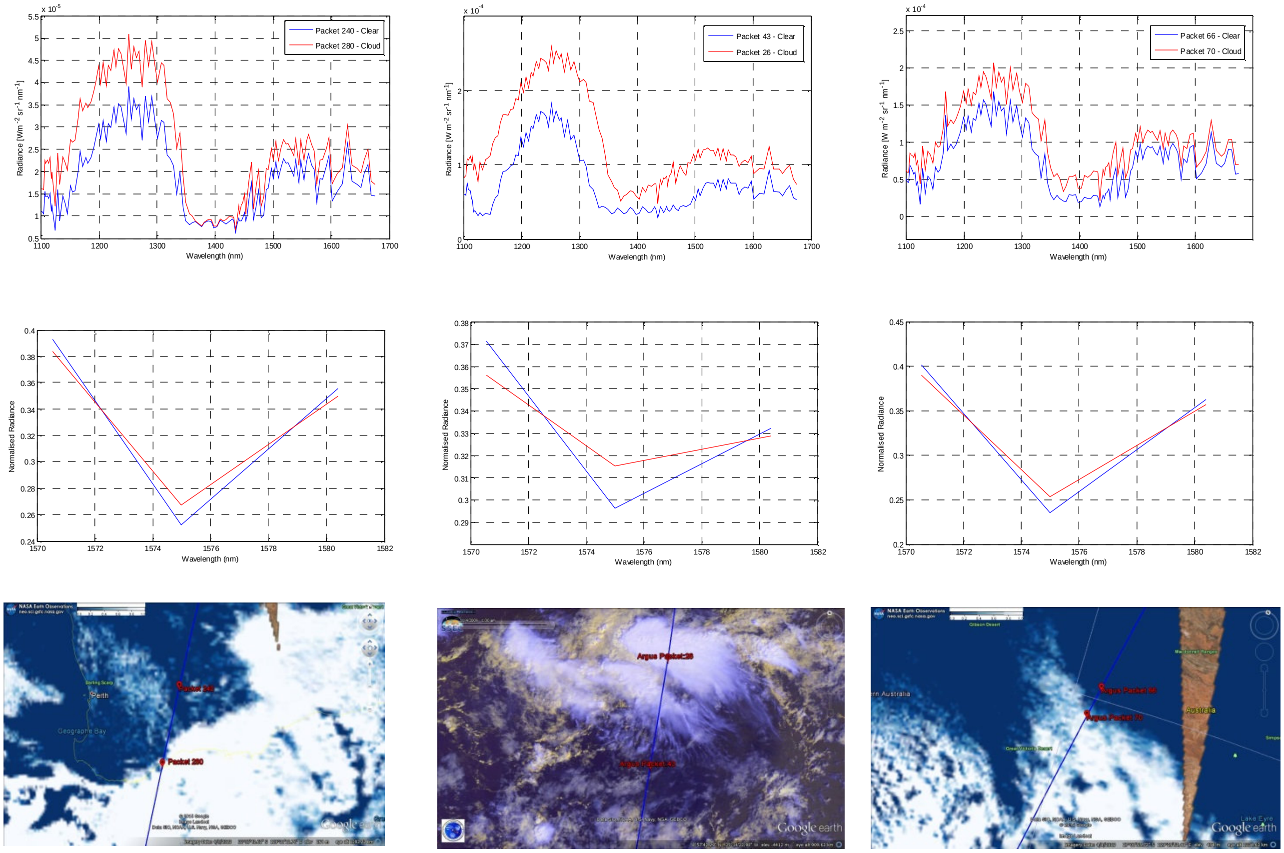

Figure 40: The full spectrum of cloudy and clear scenes (first row) for week 41 pass 34, week 9 pass 36 and week 77 pass 28, respectively. Second row shows normalized cloudy and clear spectra at the CO_2 band 1575 nm. The third row shows the actual cloud cover. [Cloud imagery by Reto Stockli, NASA's Earth Observatory http://neo.sci.gsfc.nasa.gov/]

Table 14: Geolocation details for the weeks and passes in Figure 41.

Week/Pass	Packet Number	Date	Coordinates	Status
Week 41 pass 34	240	09/09/2011	Lat: 31°41'11.40"S Long: 119°47'59.64"E	Cloud-Free
Week 41 pass 34	280	09/09/2011	Lat: 34°25'39.00"S Long: 119° 7'5.16"E	Cloudy
Week 09 pass 36	26	04/11/2009	Lat: 10°33'34.56"N Long: 34°34'12.72"W	Cloudy
Week 09 pass 36	43	04/11/2009	Lat: 8° 4'59.88"N Long: 35° 4'6.60"W	Cloud-Free
Week 77 pass 28	66	28/08/2013	Lat: 25°36'22.32"S Long: 129°56'52.08"E	Cloud-Free
Week 77 pass 28	70	28/08/2013	Lat: 26°37'45.84"S Long: 129°42'38.52"E	Cloudy

The trace gases retrieval process is performed using a forward calculation that outputs synthetic radiance profiles. Major parameters such as the gas mixing ratio profile, solar zenith angle, viewing angle, surface type, and albedo are adjusted until the best match between the synthetic and observed radiance profiles is achieved. Figure 41 shows a comparison between the simulated (model) and observed radiances at the CO_2 window 1580 nm. The observed radiance profile was collected on August 28, 2013 at latitude and longitude 14°55'19.92"S, 132°15'57.24"E, respectively. The CO_2 concentration was increased by 10% of its value in the model which is 360 ppm. This yields a CO_2 concentration of 396 ppm which is the same value recorded by the National Oceanic and Atmospheric Administration (NOAA) on August 2013 as shown in Figure 42. The parameters used in this fitting are listed in table 15.

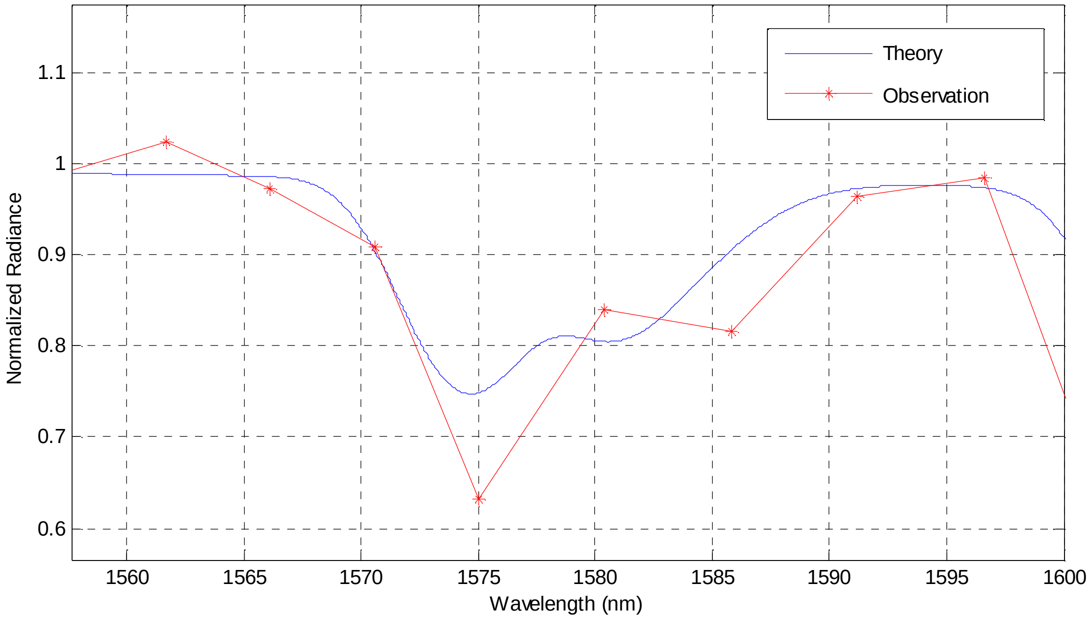

Figure 41: Synthetic (blue) and observed (red) radiance profiles.

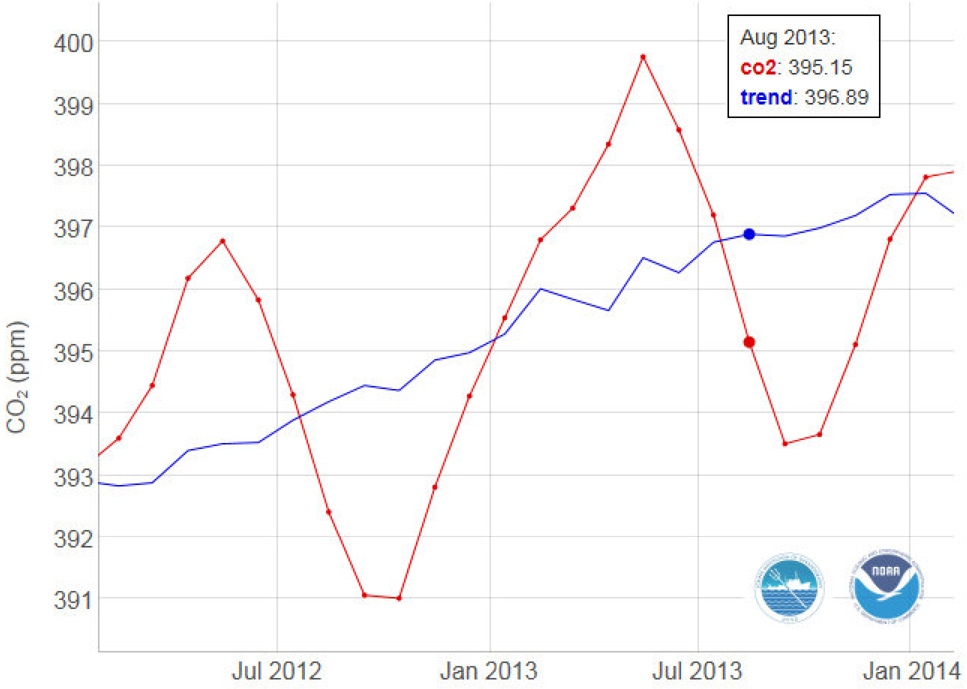

Figure 42: The CO_2 concentration level on the 28th of August 2013 as reported from the National Oceanic and Atmospheric Administration web. Graph Credit [http://www.esrl.noaa.gov/gmd/ccgg/trends/graph.html].

Table 15: Model parameters used in the fitting in Figure 42

Parameter	Value
CO_2 mixing ratio	Increased by 10%
H_2O mixing ratio	Decreased by 80.5%
Atmosphere Model	1976 U.S Standard Atmosphere
Other gases considered	Oxygen (O_2) and Methane CH_4
Height if atmosphere	50 km
SZA	50°
Viewing angle	4°
Albedo	0.4

5.0 Conclusion

A sensitivity analysis of the response of reflected solar radiation to variations in the atmospheric total carbon dioxide column was performed in this thesis. The reflected sunlight near the CO_2 absorption band 1.58 μm was investigated with respect to various parameters such as the solar zenith angle, mixing ratio of CO_2, and the albedo. The CO_2 near infrared (NIR) bands 1.58 μm and 1.60 μm are located within the Argus 1000 spectrometer spectral range, which is 1.0 to 1.7 μm. Simulations with GENSPECT results indicate that the Argus 1000 spectrometer signal-to-noise ratio (SNR) must be 2000:1 to detect 1% changes in the CO_2 mixing ratio in the atmospheric boundary layer (0-2 km). The Argus 1000 current SNR (~1520:1) can therefore yield uncertainty of approximately 1.31%. Further improvements to the SNR can be done by, for example, increasing the number of scans (co-adding setting) or performing some statistical averaging methods (spatial averaging).

The sensitivity of the back-to-space radiance to the solar zenith angle at 1.58 μm was performed at SZAs 30° and 80° at the atmospheric boundary layer where the most variability of CO_2 is located. The sensor monitors more solar radiation in small zenith angle than large zenith angle.

Two possible path scenarios of the solar photons were considered in the model to examine the total sunlight seen by the sensor. The solar radiation beam in one of the two considered scenarios was assumed to travel through longer path length than the other one in order to examine the back-to-space radiance change in each scenario. The ratio between the solar radiance reflected off ground (scenario one) and solar radiance reflected off cloud (scenario two) is approximately 4.5.

The effect of clouds on both solar radiation and CO_2 absorption is analyzed using some flight data collected by the Argus 1000 spectrometer over cloudy and cloud-free scenes. The results indicate that the CO_2 absorption in the absence of clouds is about 5.3% higher than the CO_2 absorption when clouds are present because solar photons go through longer paths in a clear sky condition, enhancing the CO_2 absorption. Photons that travel through short paths will have a lower probability to experience CO_2 absorption and thus display less strong absorption features in spectra. Generally, there is less atmospheric column path for photons in the presence of clouds but, possibly, more multi-path so these effects compete.

5.1 Future Work

Cloud and scattering models need to be incorporated in the sensitivity analysis to reduce systematic errors in the $\mathrm{CO_2}$ retrieval. With cloud and scattering models being integrated in the primary model used for the sensitivity analysis, one should be able to examine the overestimation and underestimation of the $\mathrm{CO_2}$ when solar radiation is scattered by cirrus clouds or aerosols. Hence the availability of ancillary aerosol and cloud data is important. Scattering scenarios can be more explored by assuming more possible scenarios for the photons. Clouds and snow have almost the same albedo and can become an issue when data are collected over snow on a cloudy day. There is therefore a need of discriminating clouds over snow-covered areas to properly interpret spectra.

References

Andrews, A. E., Kofler, J. D., Trudeau, M. E., Williams, J. C., Neff, D. H., Masarie, K. A., ... & Tans, P. P. (2013). CO 2, CO and CH 4 measurements from the NOAA Earth System Research Laboratory's Tall Tower Greenhouse Gas Observing Network: instrumentation, uncertainty analysis and recommendations for future high-accuracy greenhouse gas monitoring efforts. Atmospheric Measurement Techniques Discussions, 6(1), 1461-1553.

Aoki, T., Fukabori, M., & Aoki, T. (1993). Trace gas remote sounding from near IR sun glint observation with tunable etalons. In High Spectral Resolution Infrared Remote Sensing for Earth's Weather and Climate Studies (pp. 309-322). Springer Berlin Heidelberg.

Argus 1000 Owner's Manual, Thoth Technology, 2010, http://thoth.ca/spectrometers.htm

Arrhenius, S. (1896). XXXI. On the influence of carbonic acid in the air upon the temperature of the ground. The London, Edinburgh, and Dublin Philosophical Magazine and Journal of Science, 41(251), 237-276.

Aumann, H. H., & Pagano, R. J. (1994). Atmospheric infrared sounder on the Earth observing system. Optical Engineering, 33(3), 776-784.

Aumann, H. H., Chahine, M. T., Gautier, C., Goldberg, M. D., Kalnay, E., McMillin, L. M., ... & Susskind, J. (2003). AIRS/AMSU/HSB on the Aqua mission: Design, science objectives, data products, and processing systems. Geoscience and Remote Sensing, IEEE Transactions on, 41(2), 253-264.

Baker, D. F., Bösch, H., Doney, S. C., O'Brien, D., & Schimel, D. S. (2010). Carbon source/sink information provided by column CO 2 measurements from the Orbiting Carbon Observatory. Atmospheric Chemistry and Physics, 10(9), 4145-4165.

Baker, D. F., Law, R. M., Gurney, K. R., Rayner, P., Peylin, P., Denning, A. S., ... & Zhu, Z. (2006). TransCom 3 inversion intercomparison: Impact of transport model errors on the interannual variability of regional CO2 fluxes, 1988–2003. Global Biogeochemical Cycles, 20(1).

Benari, G. (2012). Geolocation algorithms for nanosatellite applications. In Masters Abstracts International (Vol. 51, No. 03).

Bernath, P. F. (2006). Atmospheric chemistry experiment (ACE): Analytical chemistry from orbit. TrAC Trends in Analytical Chemistry, 25(7), 647-654.

Bernath, P. F., McElroy, C. T., Abrams, M. C., Boone, C. D., Butler, M., Camy-Peyret, C., ... & Zou, J. (2005). Atmospheric chemistry experiment (ACE): mission overview. Geophysical Research Letters, 32(15).

Bertaux, J. L., Megie, G., Widemann, T., Chassefiere, E., Pellinen, R., Kyrola, E., ... & Simon, P. (1991). Monitoring of ozone trend by stellar occultations: The GOMOS instrument. Advances in Space Research, 11(3), 237-242.

Bodhaine, B. A., Wood, N. B., Dutton, E. G., & Slusser, J. R. (1999). On Rayleigh optical depth calculations. Journal of Atmospheric and Oceanic Technology, 16(11), 1854-1861.

Boesch, H., Baker, D., Connor, B., Crisp, D., & Miller, C. (2011). Global characterization of CO2 column retrievals from shortwave-infrared satellite observations of the Orbiting Carbon Observatory-2 mission. Remote Sensing, 3(2), 270-304.

Boland, S., Bösch, H., Brown, L., Burrows, J., Ciais, P., Connor, B., ... & Yung, Y. (2009). The need for atmospheric carbon dioxide measurements from space: contributions from a rapid reflight of the Orbiting Carbon Observatory.

Bösch, H., Toon, G. C., Sen, B., Washenfelder, R. A., Wennberg, P. O., Buchwitz, M., ... & Yung, Y. L. (2006). Space-based near-infrared CO2 measurements: Testing the Orbiting Carbon Observatory retrieval algorithm and validation concept using SCIAMACHY observations over Park Falls, Wisconsin. Journal of Geophysical Research: Atmospheres (1984–2012), 111(D23).

Bovensmann, H., Burrows, J. P., Buchwitz, M., Frerick, J., Noël, S., Rozanov, V. V., ... & Goede, A. P. H. (1999). SCIAMACHY: Mission objectives and measurement modes. Journal of the Atmospheric Sciences, 56(2), 127-150.

Bracher, A., Bovensmann, H., Bramstedt, K., Burrows, J. P., Clarmann, T. V., Eichmann, K. U., ... & Wuttke, M. W. (2005). Cross comparisons of O< sub> 3</sub> and NO< sub> 2</sub> measured by the atmospheric ENVISAT instruments GOMOS, MIPAS, and SCIAMACHY. Advances in Space Research, 36(5), 855-867.

Bréon, F. M., & Ciais, P. (2010). Spaceborne remote sensing of greenhouse gas concentrations. Comptes Rendus Geoscience, 342(4), 412-424.

Bréon, F. M., & Ciais, P. (2010). Spaceborne remote sensing of greenhouse gas concentrations. Comptes Rendus Geoscience, 342(4), 412-424.

Buchwitz, M., Beek, R. D., Burrows, J. P., Bovensmann, H., Warneke, T., Notholt, J., ... & Schulz, A. (2005). Atmospheric methane and carbon dioxide from SCIAMACHY satellite data: initial comparison with chemistry and transport models. Atmospheric Chemistry and Physics, 5(4), 941-962.

Burrows, J. P., Weber, M., Buchwitz, M., Rozanov, V., Ladstätter-Weißenmayer, A., Richter, A., ... & Perner, D. (1999). The global ozone monitoring experiment (GOME): Mission concept and first scientific results. Journal of the Atmospheric Sciences, 56(2), 151-175.

Cao, C., Xu, H., Sullivan, J., McMillin, L., Ciren, P., & Hou, Y. T. (2005). Intersatellite radiance biases for the High-Resolution Infrared Radiation Sounders (HIRS) on board NOAA-15,-16, and-17 from simultaneous nadir observations. Journal of Atmospheric and Oceanic Technology, 22(4), 381-395.

Change, IPCC Climate. "the AR4 Synthesis Report." Geneva (Suisse): IPCC (2007).

Chevallier, F., Bréon, F. M., & Rayner, P. J. (2007). Contribution of the Orbiting Carbon Observatory to the estimation of CO2 sources and sinks: Theoretical study in a variational data assimilation framework. Journal of Geophysical Research: Atmospheres (1984–2012), 112(D9).

Chevallier, F., Engelen, R. J., & Peylin, P. (2005). The contribution of AIRS data to the estimation of CO2 sources and sinks. Geophysical research letters, 32(23).

Clerbaux, C., Boynard, A., Clarisse, L., George, M., Hadji-Lazaro, J., Herbin, H., ... & Coheur, P. F. (2009). Monitoring of atmospheric composition using the thermal infrared IASI/MetOp sounder. Atmospheric Chemistry and Physics, 9(16), 6041-6054.

Crisp, D., Atlas, R. M., Breon, F. M., Brown, L. R., Burrows, J. P., Ciais, P., ... & Schroll, S. (2004). The orbiting carbon observatory (OCO) mission. Advances in Space Research, 34(4), 700-709.

Davies, R., Ridgway, W. L., & Kim, K. E. (1984). Spectral absorption of solar radiation in cloudy atmospheres: A 20 cm-1 model. Journal of the atmospheric sciences, 41(13), 2126-2137.

Dufour, E., & Bréon, F. M. (2003). Spaceborne Estimate of Atmospheric CO_2 Column by Use of the Differential Absorption Method: Error Analysis. Applied optics, 42(18), 3595-3609.

Finlayson-Pitts, B. J., & Pitts Jr, J. N. (1986). Atmospheric chemistry. Fundamentals and experimental techniques.

Forster, P., Ramaswamy, V., Artaxo, P., Berntsen, T., Betts, R., Fahey, D. W., ... & Van Dorland, R. (2007). Changes in atmospheric constituents and in radiative forcing. Chapter 2. In Climate Change 2007. The Physical Science Basis.

Funke, B., López-Puertas, M., Von Clarmann, T., Stiller, G. P., Fischer, H., Glatthor, N., ... & Wang, D. Y. (2005). Retrieval of stratospheric NOx from 5.3 and 6.2 μm nonlocal thermodynamic equilibrium emissions measured by Michelson Interferometer for Passive Atmospheric Sounding (MIPAS) on Envisat. Journal of Geophysical Research: Atmospheres (1984–2012), 110(D9).

Garand, L., Turner, D. S., Larocque, M., Bates, J., Boukabara, S., Brunel, P., ... & Woolf, H. (2001). Radiance and Jacobian intercomparison of radiative transfer models applied to HIRS and AMSU channels. Journal of Geophysical Research: Atmospheres (1984–2012), 106(D20), 24017-24031.

Hansen, J., & Sato, M. (2004). Greenhouse gas growth rates. Proceedings of the National Academy of Sciences of the United States of America, 101(46), 16109-16114.

Houweling, S., Breon, F. M., Aben, I., Rödenbeck, C., Gloor, M., Heimann, M., & Ciais, P. (2004). Inverse modeling of CO 2 sources and sinks using satellite data: a synthetic inter-comparison of measurement techniques and their performance as a function of space and time. Atmospheric Chemistry and Physics, 4(2), 523-538.

Intergovernmental Panel on Climate Change, Climate Change 2001; Synthesis Report (Cambridge U Press, New York, 2001).

IPCC (Intergovernmental Panel on Climate Change). 2014. Climate change 2014: Mitigation of climate change. Working Group III contribution to the IPCC Fifth Assessment Report. Cambridge, United Kingdom: Cambridge University Press. www.ipcc.ch/report/ar5/wg3.

Jagpal, R. K. (2011). Calibration and Validation of Argus 1000 Spectrometer–A Canadian Pollution Monitor (Doctoral dissertation, YORK UNIVERSITY, TORONTO, ONTARIO).

Jones, N. (2013). Troubling milestone for CO2. Nature Geoscience, 6(8), 589-589.

Keeling, C. D. (1973). Industrial production of carbon dioxide from fossil fuels and limestone. Tellus, 25(2), 174-198.

Kuang, Z., Margolis, J., Toon, G., Crisp, D., & Yung, Y. (2002). Spaceborne measurements of atmospheric CO2 by high-resolution NIR spectrometry of reflected sunlight: An introductory study. Geophysical Research Letters, 29(15), 11-1.

Kuze, A., Urabe, T., Suto, H., Kaneko, Y., & Hamazaki, T. (2006, August). The instrumentation and the BBM test results of thermal and near-infrared sensor for carbon observation (TANSO) on GOSAT. In SPIE Optics+ Photonics (pp. 62970K-62970K). International Society for Optics and Photonics.

Kyrölä, E., Tamminen, J., Leppelmeier, G. W., Sofieva, V., Hassinen, S., Bertaux, J. L., ... & Vanhellemont, F. (2004). GOMOS on Envisat: An overview. Advances in Space Research, 33(7), 1020-1028.

Lacis, A. A., & Oinas, V. (1991). A description of the correlated k distribution method for modeling nongray gaseous absorption, thermal emission, and multiple scattering in vertically inhomogeneous atmospheres. Journal of Geophysical Research: Atmospheres (1984–2012), 96(D5), 9027-9063.

Liou, K. N. (2002). An introduction to atmospheric radiation (Vol. 84). Academic press.

Mao, J., & Kawa, S. R. (2004). Sensitivity studies for space-based measurement of atmospheric total column carbon dioxide by reflected sunlight. Applied optics, 43(4), 914-927.

McMillin, L. M., & Fleming, H. E. (1976). model for absorbing gases with constant mixing ratios in inhomogeneous atmospheres.

Miller, C. (2011). Measuring Atmospheric Carbon Dioxide from Space. National Center for Atmospheric Research, 1-1. Retrieved March 17, 2013, from http://www.ametsoc.org/boardpges/cwce/docs/profiles/MillerCharlesE/profile.html

Miller, C. E., Crisp, D., DeCola, P. L., Olsen, S. C., Randerson, J. T., Michalak, A. M., ... & Law, R. M. (2007). Precision requirements for space-based data. Journal of Geophysical Research: Atmospheres (1984–2012), 112(D10).

NASA. The National Aeronautics and Space Administration Earth Observing System, Online http://eospso.gsfc.nasa.gov/Accessed November, 2008

Nett, H., Frerick, J., Paulsen, T., & Levrini, G. (2001). The atmospheric instruments and their applications: GOMOS, MIPAS and SCIAMACHY. ESA bulletin, 106, 77-87.

O'Brien, D. M., & Rayner, P. J. (2002). Global observations of the carbon budget, 2, CO2 column from differential absorption of reflected sunlight in the 1.61 μm band of CO2. Journal of Geophysical Research: Atmospheres (1984–2012), 107(D18), ACH-6.

Park, J. H. (1997). Atmospheric CO 2 monitoring from space. Applied optics, 36(12), 2701-2712.

Pollock, R., Haring, R. E., Holden, J. R., Johnson, D. L., Kapitanoff, A., Mohlman, D., ... & Sutin, B. M. (2010, October). The Orbiting Carbon Observatory nstrument: performance of the OCO instrument and plans for the OCO-2 instrument. In Remote Sensing (pp. 78260W-78260W). International Society for Optics and Photonics.

Qiang, F. (2002). Solar Radiaiton. Encyclopedia of Atmospheric Sciences, 1859(1863). Retrieved Mar 17, 2013, from http://www.atmos.washington.edu/~qfu/publications.php

Quine, B. M., & Drummond, J. R. (2002). GENSPECT: a line-by-line code with selectable interpolation error tolerance. Journal of Quantitative Spectroscopy and Radiative Transfer, 74(2), 147-165.

Rankin, D., Kekez, D. D., Zee, R. E., Pranajaya, F. M., Foisy, D. G., & Beattie, A. M. (2005). The CanX-2 nanosatellite: expanding the science abilities of nanosatellites. Acta Astronautica, 57(2), 167-174.

Rayner, P. J., & O'Brien, D. M. (2001). The utility of remotely sensed CO2 concentration data in surface source inversions. Geophysical research letters, 28(1), 175-178.

Rayner, P. J., Law, R. M., O'Brien, D. M., Butler, T. M., & Dilley, A. C. (2002). Global observations of the carbon budget 3. Initial assessment of the impact of satellite orbit, scan geometry, and cloud on measuring CO2 from space. Journal of Geophysical Research: Atmospheres (1984–2012), 107 (D21), ACH-2.

Sarda, K., Eagleson, S., Caillibot, E., Grant, C., Kekez, D., Pranajaya, F., & Zee, R. E. (2006). Canadian advanced nanospace experiment 2: Scientific and technological innovation on a three-kilogram satellite. Acta Astronautica, 59(1), 236-245.

Savtchenko, A., Ouzounov, D., Gopalan, A., Yuan, D., Nickless, D., & Ostrenga, D. (2003). MODIS data from Terra and Aqua satellites. In Geoscience and Remote Sensing Symposium, 2003. IGARSS'03. Proceedings. 2003 IEEE International (Vol. 5, pp. 3028-3030). IEEE.

Shi, L., Bates, J. J., & Cao, C. (2008). Scene radiance-dependent intersatellite biases of HIRS longwave channels. Journal of Atmospheric and Oceanic Technology, 25(12), 2219-2229.

Skupin, J., Noël, S., Wuttke, M. W., Gottwald, M., Bovensmann, H., Weber, M., & Burrows, J. P. (2005). SCIAMACHY solar irradiance observation in the spectral range from 240 to 2380nm. Advances in space research, 35(3), 370-375

Slingo, A., & Schrecker, H. M. (1982). On the shortwave radiative properties of stratiform water clouds. Quarterly Journal of the Royal Meteorological Society, 108(456), 407-426.

Smith, B. C. (2011). Fundamentals of Fourier transform infrared spectroscopy. CRC press.

Space Science and Engineering Centre, AVHRR (Advanced Very High Resolution Radiometer) Google Earth Imagery(2009). [Online]. Available: http://ge.ssec.wisc.edu/avhrr/

Tolton, B. T., & Plouffe, D. (2001). Sensitivity of radiometric measurements of the atmospheric CO 2 column from space. Applied optics, 40(9), 1305-1313.

Tyndall, J. (1861). The Bakerian lecture: on the absorption and radiation of heat by gases and vapours, and on the physical connexion of radiation, absorption, and conduction. Philosophical Transactions of the Royal Society of London, 151, 1-36.

von Clarmann, V., Glatthor, N., Grabowski, U., Höpfner, M., Kellmann, S., Kiefer, M., ... & López-Puertas, M. (2003). Retrieval of temperature and tangent altitude pointing from limb emission spectra recorded from space by the Michelson Interferometer for Passive Atmospheric Sounding (MIPAS). Journal of Geophysical Research: Atmospheres (1984–2012), 108(D23).

Wang, Q., Yang, Z. D., & Bi, Y. M. (2014, November). Spectral parameters and signal-to-noise ratio requirement for TANSAT hyper spectral remote sensor of atmospheric CO2. In SPIE Asia Pacific Remote Sensing (pp. 92591T-92591T). International Society for Optics and Photonics.

Warneke, T., Petersen, A. K., Gerbig, C., Jordan, A., Rödenbeck, C., Rothe, M., ... & Schrems, O. (2010). Co-located column and in situ measurements of CO 2 in the tropics compared with model simulations. Atmospheric Chemistry and Physics, 10(12), 5593-5599.

WRI (World Resources Institute). 2014. Climate Analysis Indicators Tool (CAIT) 2.0: WRI's climate data explorer. Accessed May 2014. http://cait.wri.org.

Yokota, T., Oguma, H., Morino, I., Higurashi, A., Aoki, T., & Inoue, G. (2004, December). Test measurements by a BBM of the nadir-looking SWIR FTS aboard GOSAT to monitor CO2 column density from space. In Fourth International Asia-Pacific Environmental

Remote Sensing Symposium 2004: Remote Sensing of the Atmosphere, Ocean, Environment, and Space (pp. 182-188). International Society for Optics and Photonics.